Constraining Effects of Aerosol-Cloud Interaction by Accounting for Coupling between Cloud and Land Surface

Authors
Tianning Su,[1]*† Zhanqing Li,[1]* Natalia Roldan Henao,[1] Qingzu Luan,[1] Fangqun Yu,[2]

Affiliations
[1]Earth System Science Interdisciplinary Center & AOSC, University of Maryland, USA
[2]Atmospheric Sciences Research Center, University at Albany, Albany, NY, USA
†T. Su is currently working at Lawrence Livermore National Lab

*Corresponding author. Email: Zhanqing Li, zli@atmos.umd.edu; Tianning Su, su10@llnl.gov

ABSTRACT
Aerosol-cloud interactions (ACI) are vital for regulating Earth's climate by influencing energy and water cycles. Yet, effects of ACI bear large uncertainties, evidenced by systematic discrepancies between observed and modeled estimates. This study quantifies a major bias in ACI determinations, stemming from conventional surface or space measurements that fail to capture aerosol at the cloud level unless the cloud is coupled with land surface. We introduce an advanced approach to determine radiative forcing of ACI by accounting for cloud-surface coupling. By integrating field observations, satellite data, and model simulations, this approach reveals a drastic alteration in aerosol vertical transport and ACI effects caused by cloud coupling. In coupled regimes, aerosols enhance cloud droplet number concentration across the boundary layer more homogeneously than in decoupled conditions, under which aerosols from the free atmosphere predominantly affect cloud properties, leading to marked cooling effects. Our findings spotlight cloud-surface coupling as a key factor for ACI quantification, hinting at potential under-assessments in traditional estimates.

Teaser
Accounting for cloud-land-surface coupling refines aerosol-cloud interaction estimations, altering the magnitude of their effects.

INTRODUCTION

Aerosol-cloud interactions (ACI) have been recognized as playing the central role in the regulation of the energy balance and climate of the Earth (*1-4*). By serving as cloud condensation nuclei (CCN), aerosols can regulate cloud properties and the hydrologic cycle and, thus, they exert important forcing over the radiation budget and climate change (*5-9*). However, the quantification of ACI, particularly regarding the magnitude of radiative forcing by aerosol-cloud interactions (RF_{aci}), remains highly uncertain, with substantial discrepancies persisting between observational-based estimates and modeled values (*1, 10-12*). Generally, the community tends to rely on the observation-based estimates of RF_{aci} with a global mean ranging from -0.2 to -1.0 W m^{-2} (*1, 12-14*), lower than the modeled range of -0.3 to -1.8 W m^{-2} (*2, 15*). Reconciling these differences is essential to improve the estimation of the ACI, by means of both observational analysis and model simulation (*16, 17*).

An important source of uncertainty in the quantification of RF_{aci} lies in the difficulty of the direct measurement of concentrations of cloud condensation nuclei at cloud base (*18-21*). Because measurements of CCN at the cloud level are scarce, various CCN proxy variables have been proposed and employed utilizing more conventional measurements (*13, 22-24*), including surface sulfate aerosols (*14*), aerosol optical depth (AOD) (*12, 13, 25, 26*), and aerosol extinction (*27, 28*) from which attempts were made to retrieve the CCN (*29, 30*), but their effectiveness in a wide range of conditions remains uncertain. This issue is particularly challenged by the inadequate vertical information of aerosol proxy measurements.

Previous studies have underscored the importance of aligning aerosol and cloud layers vertically for investigating the relationship between cloud microphysics and aerosol properties (*18, 31, 32*). Costantino and Bréon (*33, 34*) found that the microphysical parameters of clouds align more accurately with aerosol properties when vertical alignment is considered. Similarly, Painemal et al. (*27*) observed a stronger correlation between cloud droplet number concentration (N_d) and aerosol extinction coefficients near clouds from space-borne lidar than with AOD. Meanwhile, the N_d-CCN relationship weakens as the planetary boundary layer (PBL) deepens, suggesting that surface aerosol measurements may not effectively represent aerosol variability at the cloud base in thicker PBL (*35*). This issue was critically reviewed and summarized by Quaas et al. (*32*), noting that the lack of vertical alignment between CCN proxies and clouds leads to an underestimation of N_d-CCN sensitivity, further aggravated by the availability and uncertainties in the retrievals of vertical profiles of aerosol and cloud condensation nuclei.

Therefore, there is notable scope to refine ACI quantification by addressing the uncertainties arising from variable aerosol vertical distributions beneath clouds. We hypothesize that this challenge is intrinsically tied to cloud-surface coupling processes, which are deeply intertwined with boundary layer processes (*36*). Cloud-surface coupling refers to the exchange of turbulent fluxes between the surface and cloud through the PBL (*37, 38*). Given that most aerosols reside within the PBL, cloud-surface coupling notably influences aerosol transport from the boundary layer to the cloud base (*39*) and, in turn, ACI by modulating aerosol vertical distribution in the sub-cloud layer. While the influence of the underlying surface on ACI has been recognized (*24, 40*), quantifying RF_{aci} while considering the states of cloud-land-surface coupling remains underexplored. The recent development of a methodology to determine cloud-surface coupling (*41*) lays the groundwork for investigating this issue comprehensively.

In this study, we aim to illuminate the influence of cloud-surface coupling on aerosol structure and quantify its resulting changes in ACI estimates. This approach diverges

from existing methods that depend on lidar retrievals for assessing aerosol vertical distributions, which are limited by signal noise, cloud contamination, and sampling constraints. By integrating comprehensive observations, we examine the roles of cloud-surface coupling in aerosol transport and its impacts over the cloud properties, particularly N_d and RF_{aci} across different coupling scenarios. This comprehensive analysis leads to a framework in the estimation of RF_{aci}, with a notable advancement in narrowing down the effects of land surface coupling.

RESULTS

Impacts of cloud-surface coupling on aerosol vertical distributions

To understand the influence of cloud-surface coupling on aerosol vertical distributions, we investigated sub-cloud aerosol variations under different cloud-surface coupling conditions. Fig. 1A, derived from 627 aircraft missions conducted between 2000 and 2006 within a 15-km radius of the SGP site, displays the ratio of dry fine-mode aerosol extinction (σ_{dry}) to mean aerosol extinction within the boundary layer (σ_{PBL}) to illustrate aerosol vertical variabilities under coupled and decoupled cloud conditions. The spatial and vertical frequency of in-situ aerosol measurements are presented in fig. S1 (dataset described in *Materials and Methods*). These observations reveal distinct sub-cloud aerosol variations under coupled and decoupled regimes.

In the case of a coupled cloud, turbulences originating from the surface can extend to the cloud base, influencing cloud evolution and creating a turbulent linkage among surface, the PBL, and the cloud. In the absence of this interaction, the cloud is considered to be in a decoupled scenario. The vertical distribution of aerosol loading beneath cloud (hereafter sub-cloud) exhibits distinct differences between the coupled and decoupled regimes (two cases demonstrated in fig. S2 and fig. S3). In the coupled regime, aerosols generally mix well throughout the sub-cloud layer, evidenced by the consistent aerosol profile with smaller variabilities in Fig. 1A. Conversely, in the decoupled regime, aerosol distribution becomes heterogeneous, with a marked difference in aerosol concentrations between surface and cloud base. Weaker vertical mixing in the decoupled regime, which limits the upward transport of aerosols, accounts for this phenomenon, leading to aerosol accumulation near the surface.

In addition to the in-situ aircraft measurements, this study incorporates aerosol extinction profiles from ground-based lidars at the SGP and Beijing sites, which are free from cloud contamination. These profiles help illustrate the consistency between σ_{PBL}, σ_{cloud} (aerosol extinction at the cloud base), and AOD_{sub} (sub-cloud AOD) in coupled conditions, as well as the differences observed in decoupled scenarios (Fig. 1B-C). We also ruled out the possibility that different cloud bases notably contribute to the difference in aerosol concentrations between coupled and decoupled regimes (fig. S4). These findings underscore the substantial influence of the cloud coupling state on the aerosol vertical distribution, holding implications for quantifying ACI.

Responses of clouds to aerosols

Preceding observations suggest that substantial differences in the ACI under different states of cloud-surface coupling are rooted in different transport of aerosol from within the PBL, especially near the surface, to the cloud layer. To validate this hypothesis, we examined the influence of different aerosol proxies on cloud properties under both coupled and decoupled scenarios. As demonstrated in Fig. 2, we calculate the slopes of linear regression between the changes in N_d and the changes in aerosol proxies ($d\ ln\ N_d\ /\ d\ ln\ \alpha$), where α represents different aerosol proxies including fine-mode AOD (AOD_f) derived from the Modern-Era Retrospective analysis for Research

and Applications, version 2 (MERRA2) (*42*), the surface fine-mode aerosol extinction (diameter<1μm) or surface particulate matter with diameters ≤2.5 μm ($PM_{2.5}$) derived from in-situ measurements. We also include aerosol extinction below clouds derived from lidar, and the mean σ_{dry} within the planetary boundary layer (σ_{PBL}) and the free atmosphere (σ_{FA}) as derived from the MERRA2.

The sampling numbers for deriving the regressions in Fig. 2 are presented in fig. S5. N_d is calculated from cloud effective radius and cloud optical depth measured by the Moderate Resolution Imaging Spectroradiometer (MODIS) over Eastern Asia and the field observations over the SGP (see *Materials and Methods*). σ_{FA} is calculated as the mean σ_{dry} between the cloud-base and 600 hPa. In MERRA-2 data, conversions between aerosol mixing ratios, Particulate Matter (PM), and σ_{dry} were implemented. Despite these conversions, the responses of N_d to either PM or σ_{dry} exhibit notable similarity (Fig. S6). Our observations indicate that the overall responses of N_d to different aerosol proxies exhibit a range from 0.15 to 0.26 over the SGP and from 0.24 to 0.41 over Beijing. These findings are in general alignment with regional averages reported in previous studies, such as 0.2-0.4 over Asia and 0.1-0.5 for the North America (*12, 43*), albeit on the lower end for the latter. Furthermore, the responses of N_d to aerosols have a comparable value with global estimates of 0.2-0.4 as documented by Diamond et al. (*44*) and McCoy et al. (*14*).

Our analysis reveals that the responses of N_d to different aerosol proxies are notably different under coupled and decoupled conditions. Specifically, the N_d demonstrates substantial responses to surface aerosol extinction and AOD_f under coupled conditions, while the responses are insignificant under decoupled conditions. In contrast, the response of N_d to aerosol extinction right beneath cloud is less sensitive to the state of cloud-surface coupling. These results highlight that the states of cloud-surface coupling notably shape the sensitivity of cloud properties to different aerosol proxies, especially those measured at the surface.

The findings of our study suggest that conventional aerosol proxies, such as AOD or surface aerosol loading, are suitable for coupled regimes since there is consistency between surface aerosols, boundary layer aerosols, and aerosol loading at the cloud base. However, they fail to represent the aerosol concentration in the cloud base under decoupled conditions. Lidar-derived aerosol extinction is helpful for decoupled cloud conditions. However, lidar-derived extinction suffers from great uncertainties due to severe cloud contamination.

As a remedy solution to the potential problem, this study introduces the use of σ_{PBL} and σ_{FA} as additional aerosol proxies. The boundary layer aerosol loading provides a better representation of the aerosol extinction at the cloud base under the coupled regime (Fig. 1 and fig. S7). Conversely, the free atmosphere aerosols help gain insights into the aerosol conditions within the free atmosphere, above the boundary layer (fig. S7), and thus can be used as the aerosol proxy for the decoupled regime. These findings emphasize the importance of considering the state of cloud-surface coupling while selecting appropriate aerosol proxies for accurate ACI quantification.

RF_{aci} under coupled and decoupled conditions

By using comprehensive field observations, we present the RF_{aci} in Fig. 3 (see *Materials and Methods*). The averaged estimation of RF_{aci} by using AOD_f and surface aerosol loading as the aerosol proxies is shown by the grey bars in Fig. 3 (referred as the traditional estimation). Compared to the model simulation from GEOS-Chem (*15*), the traditional observational estimation of RF_{aci} has lower magnitude, which was the case

in previous studies (*11*, *12*, *21*). The observed discrepancies between model outputs and observational estimates could originate from various sources, e.g., variations in spatial and temporal resolutions of the datasets, temporal and vertical variations in aerosol composition, and limitations in the model's parameterization of aerosol-cloud interactions. The systematic discrepancies are likely rooted, at least partially, to the representativeness of aerosol measurements for cloud base CCN.

To quantify this, we further differentiate between coupled and decoupled regimes, revealing notable differences in the magnitude of RF_{aci} under these two states (red bars denote coupled, blue bars represent decoupled). As mentioned in the previous section, we use σ_{PBL} and σ_{FA} as the aerosol proxies for coupled and decoupled regimes, respectively. We also combined the new estimation of RF_{aci} as the aggregate of contributions from both coupled and decoupled cloud conditions, as indicated by the green bars in Fig. 3. The combined estimation of RF_{aci} is notably higher than the traditional estimation, highlighting the importance of selecting appropriate aerosol proxies according to the state of cloud-surface coupling. The calculation of RF_{aci} incorporates the relative frequency of coupled and decoupled clouds, acknowledging that the predominant occurrence of coupled clouds (approximately 70%) makes RF_{aci} is much closer to the value under the coupled scenario than decoupled scenario. The percentage of coupled and decoupled clouds at different heights are presented in fig. S8. The results emphasize the necessity of considering the cloud-surface coupling state for accurate observational-based quantification of radiative forcing instigated by aerosol-cloud interactions.

Fig. 4 shows the spatial distribution of RF_{aci} during summer over Eastern Asia for coupled and decoupled regimes, along with an overall case scenario, computed using satellite and radiosonde observational data (depicted by color dots). The state of cloud-surface coupling is determined using radiosonde data. The figure reveals substantial differences in aerosol-cloud interactions between coupled and decoupled regimes, the former being larger than the latter in magnitude. The notable differences in RF_{aci} between coupled and decoupled regimes are caused by the different responses of cloud properties for different coupling regimes (fig. S9).

In comparison, the RF_{aci} values from model simulations from the GEOS-Chem model are also portrayed by the shaded area for all cases only (Fig. 4E-F). When employing the traditional aerosol proxy, observational estimates of RF_{aci} tend to be lower than those simulated by the model, as is clear in Fig. 4E. However, using σ_{PBL} and σ_{FA} as aerosol proxies collectively account for the effects of cloud-surface coupling, making the gap between observational estimates and model simulations becomes smaller. The uncertainty that arises from the use of traditional aerosol proxies is thus reduced. This aspect is important as ACI can be modulated by the state of cloud-surface coupling. Owing to the enhanced vertical mixing within PBL, boundary layer aerosols transported to the cloud layer can effectively modulate cloud properties. In contrast, for the decoupled regime, the vertical mixing in the sub-cloud layer was suppressed, hindering the effective transport of energy, aerosol, and moisture aloft.

DISCUSSION

Our study highlights the important impact of cloud-surface coupling on ACI, a concept schematically presented in Fig. 5. Under a coupled regime, boundary layer aerosols, by facilitating the activation of more particles into cloud droplets, effectively increase N_d, reduce the droplet effective radius, and hence entail notable effects of ACI. Conversely, in a decoupled regime, inefficient transport of aerosols from PBL to the cloud base leads to disconnection between cloud optical properties and boundary layer

aerosols. It is primarily the aerosols from the free atmosphere that shape the N_d evolution under decoupled conditions.

Our discoveries shed light on the deeper intricacies of ACI processes and their radiative forcing implications. Traditional observations of RF_{aci} often blend the effects of coupled and decoupled clouds, leading to a potential bias in the quantification of ACI's radiative impact. This is particularly evident when considering the weak responsiveness of N_d to standard aerosol proxies like AOD or surface aerosol loadings in decoupled conditions. Our research introduces a methodology that circumvents the direct retrieval of aerosol vertical profiles, addressing this important uncertainty in the RF_{aci} quantification. We observed that ACI in decoupled clouds, is influenced primarily by free-atmosphere aerosols, resulting in markable cooling effects. To address this issue, we propose the use of aerosol metrics specific to the coupling state, which would offer a more accurate portrayal of cloud-surface interactions in ACI.

Observational and modeling estimates serve as the two pillars in assessing RF_{aci}. IPCC assessments synthesize ACI estimations from both these two methods, as each comes with its own set of uncertainties and can have vast variations depending on the tools and datasets in use. Our study identifies cloud-surface coupling as one of the major uncertainty factors in observational ACI evaluations. By addressing this aspect, the existing gap is narrowed considerably between observational-based and modeling-based ACI estimations. Such findings suggest a need to reevaluate our observational determination of the ACI, emphasizing the differentiation between coupled and decoupled cloud states.

It's also essential to note that observational and modeling tools are distinct entities, operating independently, which often precludes direct process-level comparisons between them. In climate models, averaged cloud properties span a 1-2° grid, characterized over daily or monthly time frames, to gauge ACI. As such outputs are not designed to discern the turbulent coupling between cloud and surface, the representation of cloud-surface coupling in climate models warrants detailed examination in the model parametrization.

Our study introduces an approach that underscores the critical role of cloud-surface coupling in ACI analysis, using specific regions as a foundational starting point, but it is infeasible to estimate its global effect. Accurate determination of cloud coupling states on a global scale poses a substantial challenge. Notably, advancements in kilometer-scale climate models (*45*) and the advent of new satellite-based lidar systems (e.g., NASA Atmosphere Observing System) (*46*) present promising opportunities for global assessments of cloud coupling. Pursuing this direction has the potential to refine ACI quantification by tackling one of its major uncertainties.

MATERIALS AND METHODS

Descriptions of datasets.

(1) Beijing and Southern Great Plains sites

This study utilizes extensive field observations obtained from a superstation in Beijing, China and observational data from the SGP observatory in Oklahoma. The measurements from the Beijing superstation encompass data gathered from ground meteorological instruments, $PM_{2.5}$ data from the surrounding area, and Micro-pulse lidar data, spanning the period of Jul. 2017 to Oct. 2019. Averaged $PM_{2.5}$ concentrations were acquired from 5 air quality monitoring sites situated within a 20-km radius of the lidar site superstation. The SGP site in Oklahoma has been a rich source of precise observational data for climate research since the late 1980s. The datasets utilized in this study from the SGP site during Oct 1998-Dec 2020 include (a) remote sensing products

of cloud boundaries (*47*), (b) vertical profiles of thermodynamic parameters, (c) ground observing system of aerosols, (d) cloud optical properties (i.e., cloud optical depth and effective radius) from the combined filed observations (Multifilter Rotating Shadowband Radiometer, Microwave Radiometer, and Langley Analysis). Since measurements of cloud properties are only available in the SGP site, we use MODIS-derived cloud optical properties over the Eastern Asia to calculate the RF_{aci}.

(2) Aircraft data over the Southern Great Plains

This study utilized in-situ aerosol extinction from the In-Situ Aerosol Profiles (IAP) campaign (https://www.arm.gov/capabilities/instruments/iap), which includes an extensive collection of 627 flight missions spanning from 2000 to 2006. We use the dry fine-mode aerosol extinction (diameter<1μm) at the green channel (σ_{dry}) from the Aerosol Observing System onboard the aircraft within a 15 km radius around the SGP site, focusing on measurements corresponding to 09-16 local times to align with the periods used for the RF_{aci} calculations.

To effectively represent the variations of aerosols in the sub-cloud layer, we normalized the measurement altitudes by the cloud base height (CBH) and calculate the mean and standard deviations of aerosol extinction at intervals of 0.1 CBH. Smoothing across each level (0.1 CBH increment) within a ±1 level window was applied to separately average profiles below and above the cloud base. Both cloud positions and PBL height (PBLH) are still obtained from the ground-based instruments to match with in-situ aerosol profiles from aircraft. The mean aerosol extinction within the boundary layer (σ_{PBL}) was computed using measurements below the PBL top within a ±1 hour window around each data point.

(3) Radiosonde stations in eastern China

We also use radiosonde stations in eastern China to illuminate the influences of coupling between cloud and land surface on ACI. The China Meteorological Administration maintains the radiosonde sites, which measured vertical profiles of temperature, wind, moisture, and pressure, and wind at 1400 Local Time (LT) during summer only. In this study, the characteristics of cloud-surface coupling were investigated using the 1400 LT soundings from 2015 to 2019, excluding days with precipitation from 1200 to 1400 LT and sites with less than 100 valid soundings at 1400 LT. The location of 13 sites can be found in Fig. 4 and fig. S9.

(4) MODIS cloud product

Due to the lack of ground measurements of cloud properties over Eastern Asia, we also use the MODIS Level-2 Cloud product, MYD06_L2 (5-Min L2 Swath 1km and 5km). MODIS-derived cloud optical depth and cloud effective radius are used to investigate the responses of cloud properties to aerosols. We use the MODIS cloud top height/temperature, cloud mask, cloud phase, liquid water path, and multilayer flag. Cloud properties are matched with ground observations within 20-km.

(5) MERRA2 reanalysis data

Since the observational AOD is generally not available during cloudy conditions, we also utilized the AOD dataset obtained from MERRA2 at a spatial resolution of $0.5^{\circ} \times 0.625^{\circ}$. Furthermore, AOD_f is defined as the aggregate of AOD for black carbon, organic aerosols, and sulfate aerosols, along with 30% of sea salt aerosols. MEERA-2 also offers the 3-hour vertical distribution of aerosol mass mixing ratio of multiple

species. The conversion from aerosol mass mixing ratio to PM and aerosol extinction (σ) is as follows:

$$PM = \sum_{x=1}^{X} r_x \times \rho_{air} \qquad (1)$$

$$\sigma = \sum_{x=1}^{X} (r_x \times \rho_{air}) \times m_x^{ext} \qquad (2)$$

where r_x is the aerosol mass mixing ratio of aerosol type x. ρ_{air} is the density of air and is provided by MERRA-2 for different atmospheric levels. m_x^{ext} is the mass extinction coefficient for aerosol type x, indicating how much light is extinguished per unit mass of the aerosol. m_x^{ext} for different aerosol species are documented in Randles et al. (*48*). We use the mass extinction coefficient at the dry condition to calculate σ_{dry}. Following the MERRA-2 official website (https://gmao.gsfc.nasa.gov/reanalysis/MERRA-2/FAQ/), we excluded the mass mixing ratio from Dust Bins 2-5 and Sea Salt Bins 3-5 for the calculation of fine-mode aerosol properties (diameter<1μm), and included 70% of Dust Bin 1. Other species except dust and sea salt are considered as fine-mode.

Table S1 compiles the necessary cloud, aerosol, as well as radiative parameters utilized for the data analyses and the computation of the RF_{aci}. We also use the Max Planck Aerosol Climatology version 2 (MACv2) to assess aerosol anthropogenic fraction (*49, 50*). The MACv2 defines monthly global maps for radiative properties and aerosol optical properties, with aerosol composition specifics derived via a top-down method that outlines the spectral aerosol single scattering properties. The determination of Anthropogenic AOD leverages scaling factors applied to the MACv2 fine-mode AOD values, which are based on model simulation results from AeroCom-Phase-2 using preindustrial (PI) and present-day (PD) emissions data.

Cloud-Surface Coupling from Lidar and Radiosonde. This study utilized a method to illuminate coupling between clouds and the land surface using remote sensing techniques (*41*), specifically lidar and radiosonde measurements. The method is based on identifying the PBLH variability (*51*) and coupled states simultaneously by analyzing both the temporal continuity and vertical profiles of backscatter within the PBL obtained from lidar. Taking into account the temporal fluctuations of the PBL, the PBLH is determined as a step signal within the function of wavelet covariance transformation and signal gradient, derived from the backscatters of lidar. Using cloud boundary product, PBLH obtained from lidar, and lifted condensation level (*52*), we differentiate clouds into coupled or decoupled clouds. Clouds are classified as coupled when the turbulent flows originating from the ground level manage to reach the base of the cloud, thereby influencing its evolution, which results in a turbulence-facilitated linkage among surface fluxes, PBL, and the cloud. For coupled clouds, we estimate the PBLH based on cloud location under cloudy conditions. The cloud top height can be regarded as the PBL top for stratiform clouds pending on conditions, and for active cumulus clouds, the cloud base height is utilized to derive the PBLH.

In addition, we assimilate radiosonde data to provide the standard identification of coupling between clouds and the land surface whenever the measurements are available. Based on the potential temperature profiles obtained from radiosonde data, we determine cloud-surface coupling. When a potential temperature inversion exists between the cloud base and the PBL top, we classify the cloud as decoupled; if no such inversion exists, we consider the cloud as coupled with the surface. Specifically, we

adopted the Liu and Liang method (*53*) to derive PBL top from radiosonde data. We implement a cloud layer identification methodology, devised by Zhang et al (*54*), that uses three distinct height-resolving relative humidity thresholds to identify the various cloud stratifications. In general, the lidar-based method shows reasonably well consistency with radiosonde-derived cloud-surface coupling with about 10% omission errors and commission errors (*41*).

Calculation of aerosol vertical distributions from lidar. Aerosol vertical distributions were calculated from the micropulse lidar over Beijing using the Klett method (*55*) to retrieve vertical profiles of aerosol extinction from the lidar signals at 532nm. The column-averaged lidar ratio, a critical parameter for retrieving extinction profiles, was normalized using AOD at 0.5 μm derived from Aerosol Robotic Network. For cloudy conditions, linear interpolation of the lidar ratio was applied. At the SGP site, we used aerosol extinction profiles from Raman lidar operating at 355nm, which provides additional constraints for retrieving aerosol extinction profiles.

To account for the substantial overlap effect near the surface (*56*), we use the aerosol extinction profiles derived from lidar above 0.3 km. The aerosol extinction coefficient was assumed to be constant within the blind zone. Accounting for multiple scattering effects, an overall uncertainty of 30% was observed during the retrieval of aerosol extinction (*57*). To estimate aerosol loading below the cloud base, we calculated the average aerosol extinctions derived from adjacent clear pixels at the cloud base height within 2-hour. To avoid cloud contamination, clear pixels are defined as those distanced more than 0.3 km from the cloud base. AOD_{sub} is determined by multiplying the mean aerosol extinction in the sub-cloud layer by either the cloud base height or 0.3 km if the cloud base resides below this threshold. Clouds introduced additional noise in the aerosol profiles; thus, we used adjacent clear-sky aerosol profiles within a 2-hour window as a proxy to analyze AOD_{sub}. If no adjacent clear-sky aerosol profiles were available, we used cloudy aerosol profiles instead.

Methodology for calculating RF_{aci}.

(1) Observational Approach

RF_{aci} is calculated based on the change in N_d since the industrial revolution (ΔN_d). We calculate the relative change of N_d from the PI era to PD using a coefficient relating $ln\ \alpha$ to $ln\ N_d$ as follows:

$$\frac{\Delta N_d}{N_d} = \left(1 - \frac{(N_d)_{PI}}{(N_d)_{PD}}\right) = \left[1 - \left(\frac{\alpha_{PI}}{\alpha_{PD}}\right)^{\beta}\right] \qquad (3)$$

where β is the $\frac{d\ ln\ N_d}{d\ ln\ \alpha}$ and is calculated as a linear regression between N_d and aerosol proxy, α. The confidence level for the linear regression was calculated using the coefficient confidence intervals from the linear model fit (*58*). α_{PI} and α_{PD} indicate the aerosol loading for the PI and PD, respectively. In this study, we use AOD_f or fine-mode aerosol extinction (σ) as the aerosol proxy to calculate the RF_{aci}. These aerosol proxies, intended to represent CCN at the cloud base, carry notable uncertainties that contribute to the overall uncertainty in estimating RF_{aci} (*32, 59*). The ratio between α_{PD} and α_{PI} is calculated as the ratio in AOD_f between PD and PI derived from MACv2 (fig. S10)

Charlson et al (*60*) proposed a method to estimate of the RF_{aci} for liquid clouds, which has been used in numerous studies (*14, 22*). They suggested that RF_{aci} ($\Delta F^{\uparrow}$) for anthropogenic aerosols can be expressed as a function of liquid water cloud fraction, f_{liq},

the cloud albedo, A_{liq}, cloud droplet number concentration, N_d, aerosol proxy, α, and daily mean down-welling solar flux, $F^{\downarrow}$.

$$\Delta F^{\uparrow} = -\frac{1}{3}F^{\downarrow}f_{liq}A_{liq}(1-A_{liq})\frac{\Delta N_d}{N_d} \qquad (4)$$

where $F^{\downarrow}$ is obtained from the European Centre for Medium-Range Weather Forecasts Reanalysis v5 (ERA-5) data (*61*). Following Segrin et al (*62*), we calculate A_{liq} as follows:

$$A_{liq} = \frac{\frac{3}{4}(1-g)\tau}{1+\frac{3}{4}(1-g)\tau} \qquad (5)$$

where τ is cloud optical depth and the asymmetry parameter g is assumed to be 0.85 (*44*).

The values of RF_{aci} for coupled and decoupled regimes also are analyzed separately in our study.

$$Coupled\ regime: (\Delta F^{\uparrow})_{coupled} = -\frac{1}{3}f_{co}F^{\downarrow}f_{liq}A_{liq}(1-A_{liq})\frac{\Delta N_d}{N_d} \qquad (6)$$

$$Decoupled\ regime: (\Delta F^{\uparrow})_{decoupled} = -\frac{1}{3}f_{de}F^{\downarrow}f_{liq}A_{liq}(1-A_{liq})\frac{\Delta N_d}{N_d} \qquad (7)$$

where f_{co} denotes the coupled fraction, which indicates the proportion of coupled clouds within liquid water clouds. f_{de} represents the decoupled fraction ($f_{de} = 1 - f_{co}$). The climatology of cloud-surface coupling and coupling fraction are represented in fig. S4 and fig. S11, respectively. A_{liq} is separately averaged for coupled and decoupled regimes. The mixture of coupled and decoupled clouds within one hour are removed. The confidence level for RF_{aci} is derived from the confidence interval of linear regression β. RF_{aci} can be considered as the sum of $(\Delta F^{\uparrow})_{coupled}$ and $(\Delta F^{\uparrow})_{decoupled}$.

To calculate RF_{aci}, an important step is the assessment of the variation in N_d as a result of anthropogenic aerosols, leveraging the relationship between N_d and α, denoted as $\frac{d\ ln\ N_d}{d\ ln\ \alpha}$. N_d is derived from the cloud effective radius and cloud optical depth for liquid water clouds, under the assumption of an adiabatic condition.

$$N_d = \gamma\tau_c^{1/2}r_e^{-5/2} \qquad (8)$$

The cloud properties are derived from field observations during 09:00-16:00 Local Time over the SGP(*63*) and are derived from Aqua MODIS over the Eastern Asia. $\frac{d\ ln\ N_d}{d\ ln\ \alpha}$ was calculated for different regions. For the Eastern Asia region, we utilize the cloud phase product from MODIS to identify and select only liquid water clouds. For the SGP region, clouds are analyzed in our analysis only when the hourly cloud top temperature exceeds 273K. The temperature profiles used to determine this criterion are sourced from ERA-5. For more reliable fitting parameters, statistical regressions are performed using a subset of data that exhibits lower retrieval inaccuracies. Following the previous studies (*12, 22, 64*), our analyses exclude the retrievals involving multilayered clouds (MODIS product), thin clouds (liquid water path, L < 20 g m^{-2}), and possible precipitable clouds (L > 200 g m^{-2}). Furthermore, the bottom 15% of data for aerosol loading (α) are also excluded due to the sensitivity of the slopes of $In\ N_d$ versus $In\ \alpha$ to minimal aerosol variations. These minor changes have notably large retrieval uncertainties for both AOD and aerosol extinction (*12, 65*). As for the calculation of RF_{aci}, all liquid water clouds are used to calculate the liquid water cloud fraction and the cloud optical depth (*12, 21*). All datasets are averaged with an hourly resolution. Due to the data availability, we rely on cloud properties obtained from MODIS measurements over the Eastern Asian during the daytime.

(2) Modeling output

This study also directly utilized the output of RF_{aci} from the work of Yu et al. (*15*), which integrates a size-resolved advanced particle microphysics (APM) model and the Rapid Radiative Transfer Model for GCMs (RRTMG) for shortwave radiation with the GEOS-Chem model. This modeling approach explicitly simulates the formation, growth, and atmospheric processing of secondary and primary aerosols, including sulfate, nitrate, ammonium, secondary organic aerosol, black carbon, primary organic carbon, dust, and sea salt particles. This modeling approach assesses aerosol impacts on cloud albedo and solar radiation by comparing simulations with present-day emissions against pre-industrial conditions. The approach for estimating RF_{aci} follows IPCC guidelines, isolating the effect of increased aerosol concentration on cloud optical properties and top-of-atmosphere solar fluxes, without considering feedback mechanisms.

Supplementary Materials

This PDF file includes:

Figs. S1 to S11

Table S1

Reference

1. O. Boucher, D. Randall, P. Artaxo, C. Bretherton, G. Feingold, P. Forster, V.-M. Kerminen, Y. Kondo, H. Liao, U. Lohmann, "Clouds and aerosols" in *Climate change 2013: the physical science basis. Contribution of Working Group I to the Fifth Assessment Report of the Intergovernmental Panel on Climate Change* (Cambridge University Press, 2013), pp. 571-657.
2. S. Solomon, D. Qin, M. Manning, K. Averyt, M. Marquis, *Climate change 2007-the physical science basis: Working group I contribution to the fourth assessment report of the IPCC* (Cambridge university press, 2007), vol. 4.
3. V. Masson-Delmotte, P. Zhai, A. Pirani, S. L. Connors, C. Péan, S. Berger, N. Caud, Y. Chen, L. Goldfarb, M. Gomis, Climate change 2021: the physical science basis. *Contribution of working group I to the sixth assessment report of the intergovernmental panel on climate change* **2**, (2021).
4. F. F. Malavelle, J. M. Haywood, A. Jones, A. Gettelman, L. Clarisse, S. Bauduin, R. P. Allan, I. H. H. Karset, J. E. Kristjánsson, L. Oreopoulos, Strong constraints on aerosol–cloud interactions from volcanic eruptions. *Nature* **546**, 485-491 (2017).
5. S. Twomey, Pollution and the planetary albedo. *Atmospheric Environment (1967)* **8**, 1251-1256 (1974).
6. B. A. Albrecht, Aerosols, cloud microphysics, and fractional cloudiness. *Science* **245**, 1227-1230 (1989).
7. Z. Li, W. M. Lau, V. Ramanathan, G. Wu, Y. Ding, M. Manoj, J. Liu, Y. Qian, J. Li, T. Zhou, Aerosol and monsoon climate interactions over Asia. *Reviews of Geophysics* **54**, 866-929 (2016).
8. Z. Li, F. Niu, J. Fan, Y. Liu, D. Rosenfeld, Y. Ding, Long-term impacts of aerosols on the vertical development of clouds and precipitation. *Nature Geoscience* **4**, 888-894 (2011).
9. R. Wood, M. Wyant, C. S. Bretherton, J. Rémillard, P. Kollias, J. Fletcher, J. Stemmler, S. De Szoeke, S. Yuter, M. Miller, Clouds, aerosols, and precipitation in the marine boundary layer: An arm mobile facility deployment. *Bulletin of the American Meteorological Society* **96**, 419-440 (2015).
10. U. Lohmann, G. Lesins, Stronger constraints on the anthropogenic indirect aerosol effect. *Science* **298**, 1012-1015 (2002).

11. N. Bellouin, J. Quaas, E. Gryspeerdt, S. Kinne, P. Stier, D. Watson-Parris, O. Boucher, K. S. Carslaw, M. Christensen, A. L. Daniau, J. L. Dufresne, G. Feingold, S. Fiedler, P. Forster, A. Gettelman, J. M. Haywood, U. Lohmann, F. Malavelle, T. Mauritsen, D. T. McCoy, G. Myhre, J. Mulmenstadt, D. Neubauer, A. Possner, M. Rugenstein, Y. Sato, M. Schulz, S. E. Schwartz, O. Sourdeval, T. Storelvmo, V. Toll, D. Winker, B. Stevens, Bounding Global Aerosol Radiative Forcing of Climate Change. *Reviews of Geophysics* **58**, (2020).
12. H. Jia, X. Ma, F. Yu, J. Quaas, Significant underestimation of radiative forcing by aerosol–cloud interactions derived from satellite-based methods. *Nature communications* **12**, 3649 (2021).
13. J. Quaas, O. Boucher, N. Bellouin, S. Kinne, Satellite-based estimate of the direct and indirect aerosol climate forcing. *Journal of Geophysical Research: Atmospheres* **113**, (2008).
14. D. McCoy, F. M. Bender, J. Mohrmann, D. Hartmann, R. Wood, D. Grosvenor, The global aerosol-cloud first indirect effect estimated using MODIS, MERRA, and AeroCom. *Journal of Geophysical Research: Atmospheres* **122**, 1779-1796 (2017).
15. F. Yu, X. Ma, G. Luo, Anthropogenic contribution to cloud condensation nuclei and the first aerosol indirect climate effect. *Environmental Research Letters* **8**, 024029 (2013).
16. Y.-C. Chen, M. W. Christensen, G. L. Stephens, J. H. Seinfeld, Satellite-based estimate of global aerosol–cloud radiative forcing by marine warm clouds. *Nat Geosci* **7**, 643-646 (2014).
17. J. E. Penner, L. Xu, M. Wang, Satellite methods underestimate indirect climate forcing by aerosols. *Proceedings of the National Academy of Sciences* **108**, 13404-13408 (2011).
18. D. Rosenfeld, Y. Zheng, E. Hashimshoni, M. L. Pöhlker, A. Jefferson, C. Pöhlker, X. Yu, Y. Zhu, G. Liu, Z. Yue, Satellite retrieval of cloud condensation nuclei concentrations by using clouds as CCN chambers. *Proceedings of the National Academy of Sciences* **113**, 5828-5834 (2016).
19. D. Rosenfeld, Aerosol-driven droplet concentrations dominate coverage and water of oceanic low-level clouds (vol 364, eaay4194, 2019). *Science* **365**, 230-230 (2019).
20. J. Fan, Y. Wang, D. Rosenfeld, X. Liu, Review of aerosol–cloud interactions: Mechanisms, significance, and challenges. *Journal of the Atmospheric Sciences* **73**, 4221-4252 (2016).
21. J. Quaas, Approaches to observe anthropogenic aerosol-cloud interactions. *Current climate change reports* **1**, 297-304 (2015).
22. E. Gryspeerdt, J. Quaas, S. Ferrachat, A. Gettelman, S. Ghan, U. Lohmann, H. Morrison, D. Neubauer, D. G. Partridge, P. Stier, Constraining the instantaneous aerosol influence on cloud albedo. *Proceedings of the National Academy of Sciences* **114**, 4899-4904 (2017).
23. M. W. Christensen, A. Gettelman, J. Cermak, G. Dagan, M. Diamond, A. Douglas, G. Feingold, F. Glassmeier, T. Goren, D. P. Grosvenor, Opportunistic experiments to constrain aerosol effective radiative forcing. *Atmospheric chemistry and physics* **22**, 641-674 (2022).
24. X. Zheng, B. Xi, X. Dong, T. Logan, Y. Wang, P. Wu, Investigation of aerosol–cloud interactions under different absorptive aerosol regimes using Atmospheric Radiation Measurement (ARM) southern Great Plains (SGP)

ground-based measurements. *Atmos Chem Phys* **20**, 3483-3501 (2020).
25. J. Liu, Z. Li, Estimation of cloud condensation nuclei concentration from aerosol optical quantities: influential factors and uncertainties. *Atmospheric Chemistry and Physics* **14**, 471-483 (2014).
26. V. Toll, M. Christensen, J. Quaas, N. Bellouin, Weak average liquid-cloud-water response to anthropogenic aerosols. *Nature* **572**, 51-55 (2019).
27. D. Painemal, F.-L. Chang, R. Ferrare, S. Burton, Z. Li, W. L. Smith Jr, P. Minnis, Y. Feng, M. Clayton, Reducing uncertainties in satellite estimates of aerosol–cloud interactions over the subtropical ocean by integrating vertically resolved aerosol observations. *Atmospheric chemistry and physics* **20**, 7167-7177 (2020).
28. N. Wang, K. Zhang, X. Shen, Y. Wang, J. Li, C. Li, J. Mao, A. Malinka, C. Zhao, L. M. Russell, Dual-field-of-view high-spectral-resolution lidar: Simultaneous profiling of aerosol and water cloud to study aerosol–cloud interaction. *Proceedings of the National Academy of Sciences* **119**, e2110756119 (2022).
29. S. J. Ghan, T. A. Rissman, R. Elleman, R. A. Ferrare, D. Turner, C. Flynn, J. Wang, J. Ogren, J. Hudson, H. H. Jonsson, Use of in situ cloud condensation nuclei, extinction, and aerosol size distribution measurements to test a method for retrieving cloud condensation nuclei profiles from surface measurements. *Journal of Geophysical Research: Atmospheres* **111**, (2006).
30. M. Lv, Z. Wang, Z. Li, T. Luo, R. Ferrare, D. Liu, D. Wu, J. Mao, B. Wan, F. Zhang, Retrieval of cloud condensation nuclei number concentration profiles from lidar extinction and backscatter data. *Journal of Geophysical Research: Atmospheres* **123**, 6082-6098 (2018).
31. R.-E. Mamouri, A. Ansmann, Potential of polarization lidar to provide profiles of CCN-and INP-relevant aerosol parameters. *Atmospheric Chemistry and Physics* **16**, 5905-5931 (2016).
32. J. Quaas, A. Arola, B. Cairns, M. Christensen, H. Deneke, A. M. Ekman, G. Feingold, A. Fridlind, E. Gryspeerdt, O. Hasekamp, Constraining the Twomey effect from satellite observations: issues and perspectives. *Atmospheric Chemistry and Physics* **20**, 15079-15099 (2020).
33. L. Costantino, F. M. Bréon, Analysis of aerosol-cloud interaction from multi-sensor satellite observations. *Geophysical Research Letters* **37**, (2010).
34. L. Costantino, F.-M. Bréon, Aerosol indirect effect on warm clouds over South-East Atlantic, from co-located MODIS and CALIPSO observations. *Atmospheric Chemistry and Physics* **13**, 69-88 (2013).
35. D. Painemal, J. Y. C. Chiu, P. Minnis, C. Yost, X. Zhou, M. Cadeddu, E. Eloranta, E. R. Lewis, R. Ferrare, P. Kollias, Aerosol and cloud microphysics covariability in the northeast Pacific boundary layer estimated with ship-based and satellite remote sensing observations. *Journal of Geophysical Research: Atmospheres* **122**, 2403-2418 (2017).
36. T. Su, Z. Li, Y. Zheng, Cloud-Surface Coupling Alters the Morning Transition From Stable to Unstable Boundary Layer. *Geophysical Research Letters* **50**, e2022GL102256 (2023).
37. C. Jones, C. Bretherton, D. Leon, Coupled vs. decoupled boundary layers in VOCALS-REx. *Atmospheric Chemistry and Physics* **11**, 7143-7153 (2011).
38. S. Nicholls, The dynamics of stratocumulus: Aircraft observations and comparisons with a mixed layer model. *Quarterly Journal of the Royal*

Meteorological Society **110**, 783-820 (1984).
39. H. J. Griesche, K. Ohneiser, P. Seifert, M. Radenz, R. Engelmann, A. Ansmann, Contrasting ice formation in Arctic clouds: surface-coupled vs. surface-decoupled clouds. *Atmospheric Chemistry and Physics* **21**, 10357-10374 (2021).
40. L. Delle Monache, K. D. Perry, R. T. Cederwall, J. A. Ogren, In situ aerosol profiles over the Southern Great Plains cloud and radiation test bed site: 2. Effects of mixing height on aerosol properties. *Journal of Geophysical Research: Atmospheres* **109**, (2004).
41. T. Su, Y. Zheng, Z. Li, Methodology to determine the coupling of continental clouds with surface and boundary layer height under cloudy conditions from lidar and meteorological data. *Atmos Chem Phys* **22**, 1453-1466 (2022).
42. R. Gelaro, W. McCarty, M. J. Suárez, R. Todling, A. Molod, L. Takacs, C. A. Randles, A. Darmenov, M. G. Bosilovich, R. Reichle, The modern-era retrospective analysis for research and applications, version 2 (MERRA-2). *Journal of climate* **30**, 5419-5454 (2017).
43. X. Ma, F. Yu, J. Quaas, Reassessment of satellite-based estimate of aerosol climate forcing. *Journal of Geophysical Research: Atmospheres* **119**, 10,394-310,409 (2014).
44. M. S. Diamond, H. M. Director, R. Eastman, A. Possner, R. Wood, Substantial cloud brightening from shipping in subtropical low clouds. *AGU Advances* **1**, e2019AV000111 (2020).
45. P. M. Caldwell, C. R. Terai, B. Hillman, N. D. Keen, P. Bogenschutz, W. Lin, H. Beydoun, M. Taylor, L. Bertagna, A. Bradley, Convection-permitting simulations with the E3SM global atmosphere model. *Journal of Advances in Modeling Earth Systems* **13**, e2021MS002544 (2021).
46. S. A. Braun, J. Yorks, T. Thorsen, D. Cecil, D. Kirschbaum, in *IGARSS 2022-2022 IEEE International Geoscience and Remote Sensing Symposium*. (IEEE, 2022), pp. 7391-7393.
47. E. E. Clothiaux, T. P. Ackerman, G. G. Mace, K. P. Moran, R. T. Marchand, M. A. Miller, B. E. Martner, Objective determination of cloud heights and radar reflectivities using a combination of active remote sensors at the ARM CART sites. *Journal of Applied Meteorology and Climatology* **39**, 645-665 (2000).
48. C. Randles, A. Da Silva, V. Buchard, P. Colarco, A. Darmenov, R. Govindaraju, A. Smirnov, B. Holben, R. Ferrare, J. Hair, The MERRA-2 aerosol reanalysis, 1980 onward. Part I: System description and data assimilation evaluation. *Journal of climate* **30**, 6823-6850 (2017).
49. S. Kinne, The MACv2 aerosol climatology. *Tellus B: Chemical and Physical Meteorology* **71**, 1-21 (2019).
50. B. Stevens, S. Fiedler, S. Kinne, K. Peters, S. Rast, J. Müsse, S. J. Smith, T. Mauritsen, MACv2-SP: A parameterization of anthropogenic aerosol optical properties and an associated Twomey effect for use in CMIP6. *Geoscientific Model Development* **10**, 433-452 (2017).
51. T. Su, Z. Li, R. Kahn, A new method to retrieve the diurnal variability of planetary boundary layer height from lidar under different thermodynamic stability conditions. *Remote Sensing of Environment* **237**, 111519 (2020).
52. D. M. Romps, Exact expression for the lifting condensation level. *Journal of the Atmospheric Sciences* **74**, 3891-3900 (2017).
53. S. Liu, X.-Z. Liang, Observed diurnal cycle climatology of planetary boundary layer height. *Journal of Climate* **23**, 5790-5809 (2010).

54. J. Zhang, Z. Li, H. Chen, M. Cribb, Validation of a radiosonde-based cloud layer detection method against a ground-based remote sensing method at multiple ARM sites. *Journal of Geophysical Research: Atmospheres* **118**, 846-858 (2013).
55. J. D. Klett, Lidar Inversion with Variable Backscatter Extinction Ratios. *Applied Optics* **24**, 1638-1643 (1985).
56. A. Ansmann, M. Riebesell, U. Wandinger, C. Weitkamp, E. Voss, W. Lahmann, W. Michaelis, Combined Raman elastic-backscatter lidar for vertical profiling of moisture, aerosol extinction, backscatter, and lidar ratio. *Applied Physics B* **55**, 18-28 (1992).
57. Q. S. He, C. C. Li, J. T. Mao, A. K. H. Lau, P. R. Li, A study on the aerosol extinction-to-backscatter ratio with combination of micro-pulse LIDAR and MODIS over Hong Kong. *Atmospheric Chemistry and Physics* **6**, 3243-3256 (2006).
58. J. Sun, C. R. Loader, Simultaneous confidence bands for linear regression and smoothing. *The Annals of Statistics*, 1328-1345 (1994).
59. P. Stier, Limitations of passive remote sensing to constrain global cloud condensation nuclei. *Atmospheric Chemistry and Physics* **16**, 6595-6607 (2016).
60. R. J. Charlson, S. Schwartz, J. Hales, R. D. Cess, J. Coakley Jr, J. Hansen, D. Hofmann, Climate forcing by anthropogenic aerosols. *Science* **255**, 423-430 (1992).
61. H. Hersbach, B. Bell, P. Berrisford, S. Hirahara, A. Horányi, J. Muñoz-Sabater, J. Nicolas, C. Peubey, R. Radu, D. Schepers, The ERA5 global reanalysis. *Quarterly Journal of the Royal Meteorological Society* **146**, 1999-2049 (2020).
62. M. S. Segrin, J. A. Coakley Jr, W. R. Tahnk, MODIS observations of ship tracks in summertime stratus off the west coast of the United States. *Journal of the Atmospheric Sciences* **64**, 4330-4345 (2007).
63. D. D. Turner, S. McFarlane, L. Riihimaki, Y. Shi, C. Lo, Q. Min, "Cloud Optical Properties from the Multifilter Shadowband Radiometer (MFRSRCLDOD). An ARM Value-Added Product" (DOE ARM Climate Research Facility, Washington, DC (United States), 2014).
64. O. P. Hasekamp, E. Gryspeerdt, J. Quaas, Analysis of polarimetric satellite measurements suggests stronger cooling due to aerosol-cloud interactions. *Nature communications* **10**, 5405 (2019).
65. A. Arola, A. Lipponen, P. Kolmonen, T. H. Virtanen, N. Bellouin, D. P. Grosvenor, E. Gryspeerdt, J. Quaas, H. Kokkola, Aerosol effects on clouds are concealed by natural cloud heterogeneity and satellite retrieval errors. *Nature Communications* **13**, 7357 (2022).

Acknowledgments

We thank the useful discussions with Prof. Youtong Zheng and Prof. Daniel Rosenfeld.

Funding: This research was supported by:
National Science Foundation grant AGS2126098
Department of Energy's Atmospheric System Research program grant DE-SC0022919
National Aeronautics and Space Administration grant 80NSSC19K1275
Work at LLNL is performed under the auspices of the U.S. DOE by LLNL under Contract DE-AC52-07NA27344.

Author contributions: Conceptualization: TS, ZL, NRH
Methodology: TS, ZL
Investigation: TS, NRH, QL, FY
Visualization: TS
Supervision: ZL
Validation: TS, ZL
Funding acquisition: ZL
Project administration: TS, ZL
Writing—original draft: TS
Writing—review & editing: TS, NRH, FY
Resources: TS, FY
Data curation: TS, FY
Formal analysis: TS, NRH
Software: TS, NRH

Competing interests: The authors declare no competing interests.

Data and materials availability: Public access to ARM data is facilitated through the Atmospheric Radiation Measurement Data Center at this URL: https://www.arm.gov/capabilities/instruments/. Aircraft data during the In-Situ Aerosol Profiles (IAP) campaign can be found in https://doi.org/10.5439/1992437. The MODIS Cloud Properties product can be found at the following web address: https://ladsweb.modaps.eosdis.nasa.gov/missions-and-measurements/products/CLDPROP_L2_MODIS_Aqua/. The MERRA-2 reanalysis product can be accessed here: https://goldsmr4.gesdisc.eosdis.nasa.gov/data/MERRA2/. Radiosonde data along with surface meteorological measurements are published by China Meteorological Administration's National Meteorological Information Centre: http://data.cma.cn/en/?r=data/index&cid=e6ba725cabfddf8b. Lidar data over Beijing are available at http://doi.org/10.5281/zenodo.5639046/. The MACv2 aerosol climatology product is accessible via this FTP site: ftp://ftp-projects.zmaw.de/aerocom/climatology/MACv2_2018/, and for convenient access, it is also available in a permanent repository: https://doi.org/10.5281/zenodo.10691456. All data are available in the main text or the supplementary materials

Figures

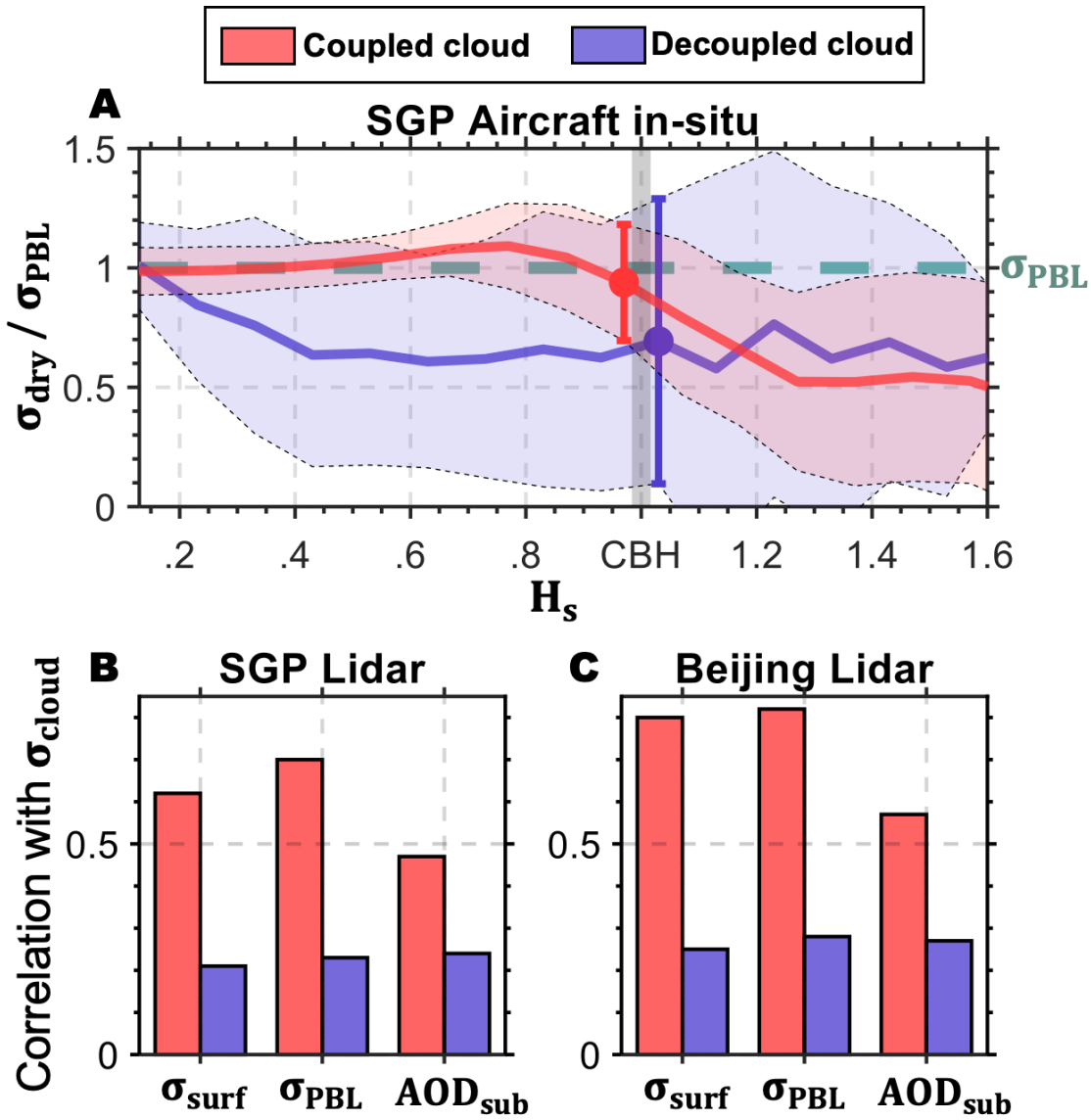

Fig. 1. Sub-cloud aerosol variations under coupled and decoupled regimes. (A) Normalized aerosol extinction profiles measured by aircraft in-situ within 15-km around the Southern Great Plains (SGP) site. Solid lines represent the ratio of dry fine-mode aerosol extinction (σ_{dry}) to mean aerosol extinction within the boundary layer (σ_{PBL}) as a function of Normalized Height (H_s), where H_s is defined as the height divided by the cloud base height (CBH). The shaded areas indicate the standard deviation of $\sigma_{dry}/\sigma_{PBL}$, with different colors representing coupled (red) and decoupled (blue) cloud conditions. The error-bars represent the stand deviations of $\sigma_{dry}/\sigma_{PBL}$ near the cloud-base. (B) Correlation coefficients between aerosol extinction at the cloud base height (σ_{cloud}) and different aerosol indexes, including near-surface aerosol extinction (σ_{surf}), σ_{PBL}, and sub-cloud aerosol optical depth (AOD_{sub}) derived from ground-based lidar measurements over (B) the SGP and (C) Beijing. σ_{cloud} is computed as the mean extinction from neighboring clear pixels at the cloud base height.

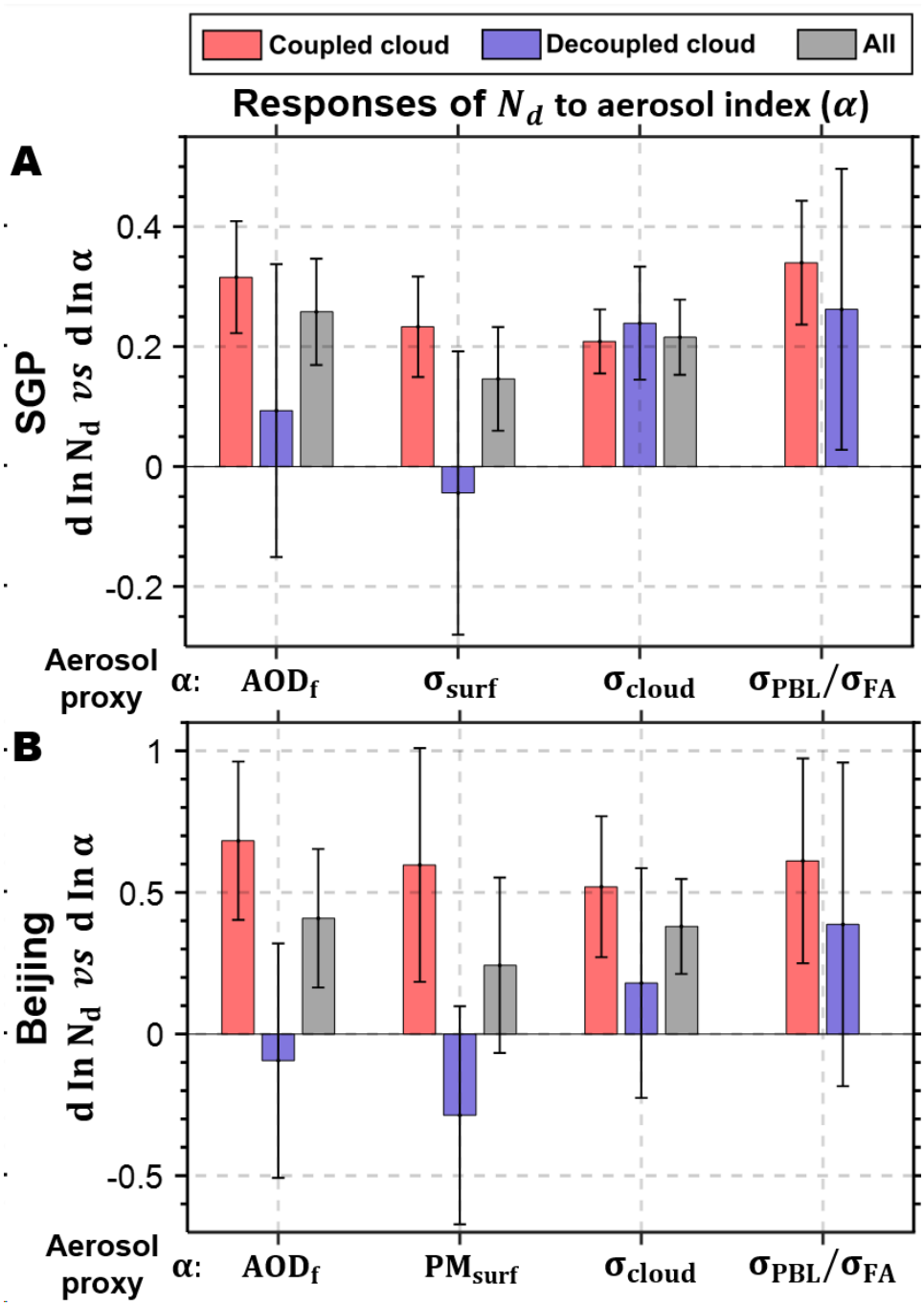

Fig. 2. The responses of cloud droplet number concentration to aerosol under different coupling regimes. The responses ($\frac{d\ ln\ N_d}{d\ ln\ \alpha}$) are calculated as the slopes of linear regression between $d\ ln\ N_d$ and $d\ ln\ \alpha$ for liquid water clouds over (A) SGP and (B) Beijing. Red, blue, and grey bars indicate the responses for coupled cases, decoupled cases, and all cases. The aerosol proxies used are fine-mode aerosol optical depth (AOD_f) derived from MERRA-2, the surface fine-mode (diameter<1μm) aerosol extinction (fine-mode σ_{surf}), surface $PM_{2.5}$ derived from in-situ measurements, aerosol extinction below clouds derived from lidar (σ_{cloud}), and mean σ_{dry} within PBL (σ_{PBL}) and mean σ_{dry} within free atmosphere (σ_{FA}) derived from MERRA-2. σ_{FA} is calculated as the mean σ_{dry} between cloud-base and 600 hPa. The error-bars indicate the 90% confidence level.

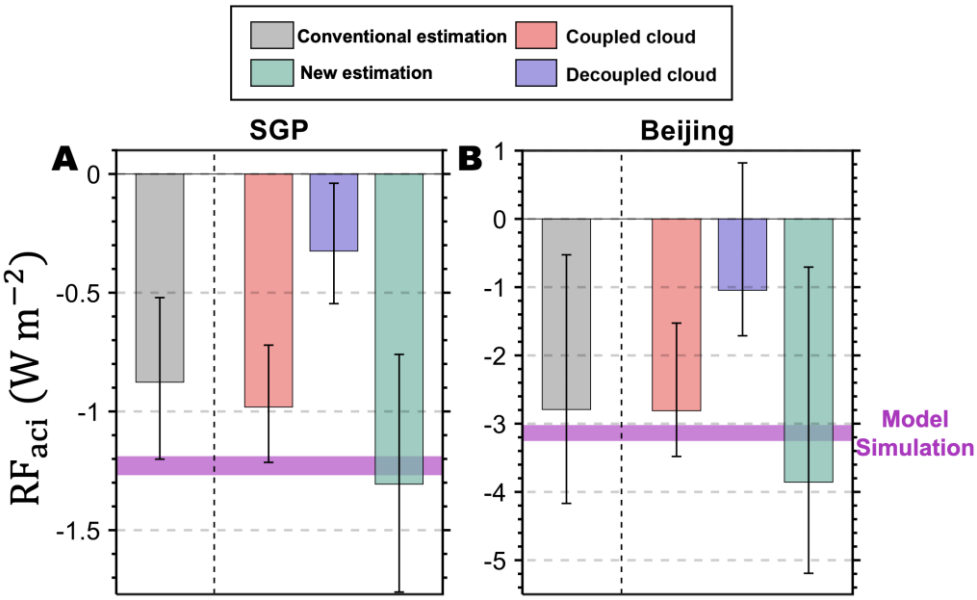

Fig. 3. Comparative radiative forcing caused by aerosol-cloud interactions (RF_{aci}) under different coupling regimes. The grey bars indicate the averaged estimation (traditional estimation) of RF_{aci} by using AOD_f and surface aerosol loading as the aerosol proxies. We also separately consider the coupled (red bars) and decoupled (blue bars) regimes. In the coupled regime, σ_{PBL} is used as the aerosol proxy, while aerosol extinction below σ_{FA} is used as the aerosol proxy in the decoupled regime. The green bars indicate the consolidated new estimation. The error-bars indicate the 90% confidence level. For comparison, the pink line indicates the value of RF_{aci} from the GEOS-Chem model (*15*).

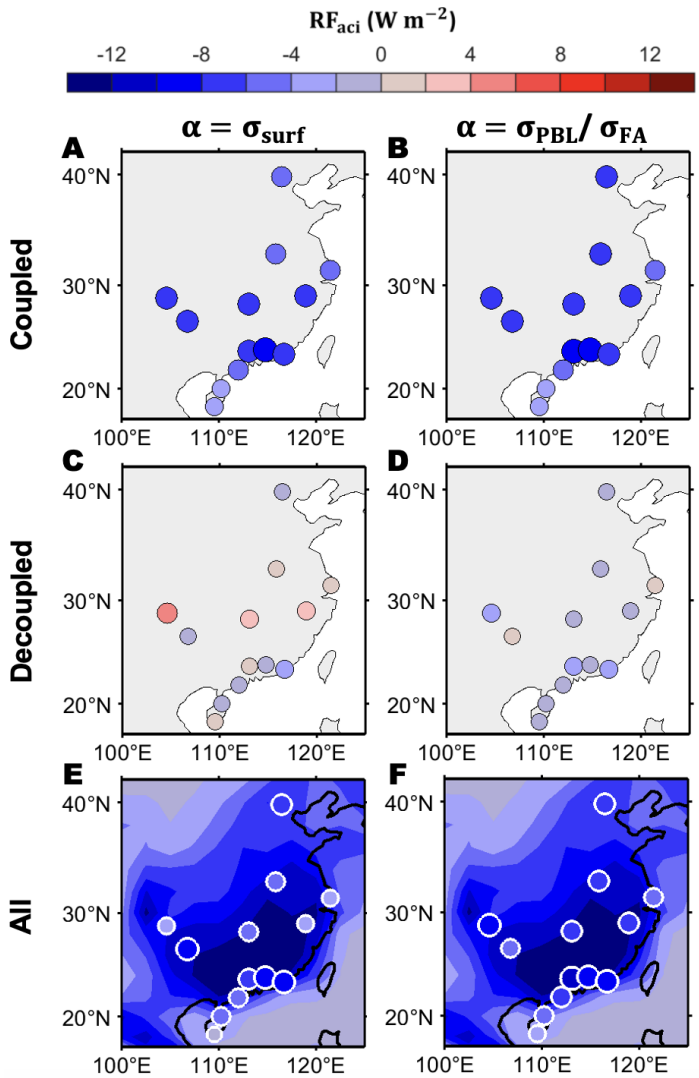

Fig. 4. Summer RF_{aci} over Eastern Asia. The dots are color-coded based on the RF_{aci} calculated from satellite estimations over radiosonde sites during summer for (A, B) coupled condition, (C, D) decoupled condition, and (E, F) all. The size of dots is adjusted according to the magnitude. The color shaded area in (E, F) represents the summer values of model simulations from the GEOS-Chem model(*15*). In (A, C, E), we use surface level σ_{dry} as the aerosol proxy. In (B, D, F), we use σ_{PBL} and σ_{FA} as aerosol proxies for coupled and decoupled regimes, respectively. The state of cloud-surface coupling is diagnosed by radiosonde data. Observational RF_{aci} is calculated during the summertime of 2015-2019 due to the availability of noontime radiosonde.

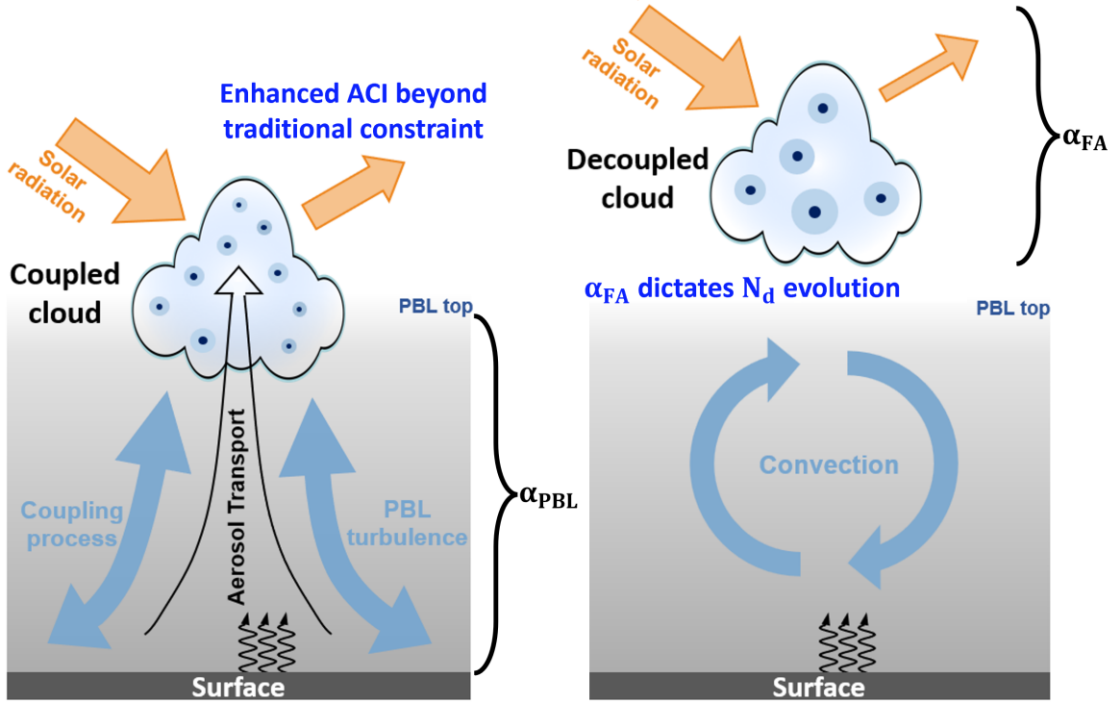

Fig. 5. A schematic diagram describing the impacts of cloud coupling on ACI. Orange arrows represent solar radiation. The grey shaded area indicates boundary layer aerosols. Black, curved arrows indicate surface heat fluxes. The coupling process, bridging clouds and the land surface, propels the vertical ascent of humidity, aerosols, and heat fluxes from the PBL up to the clouds (illustrated by the background black arrow). α_{PBL} and α_{FA}, representing the aerosol loading within PBL and within free atmosphere, can be used as the aerosol proxies for coupled and decoupled regimes, respectively. Under the coupling regime, boundary layer aerosols cause a notable cooling effect through changing the cloud albedo. Under the decoupled regime, free atmosphere aerosols dictate the variations in N_d. As a net result, neglecting cloud coupling can result in an underestimation of aerosol indirect radiative forcing.

Science Advances
AAAS

Supplementary Materials for

Constraining Effects of Aerosol-Cloud Interaction by Accounting for Coupling between Cloud and Land Surface

Tianning Su *et al.*

*Corresponding author. Email: Tianning Su, su10@llnl.gov; Zhanqing Li, zli@atmos.umd.edu;

This PDF file includes:

Figs. S1 to S11
Table S1

Supplementary Materials

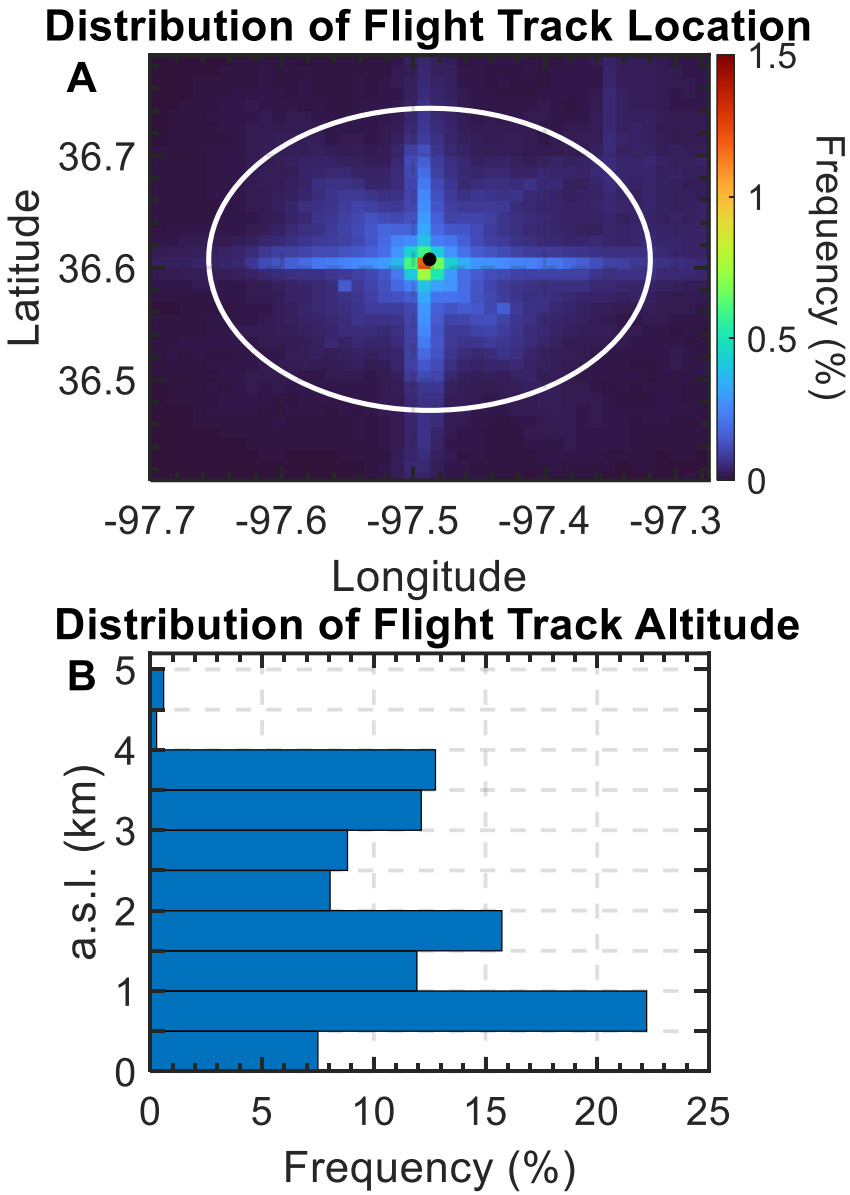

Fig. S1. Spatial and vertical sampling frequency of aerosol measurements from aircraft missions. (A) Heatmap of aircraft sampling frequency over the Southern Great Plains, showing the geographical frequency of flight paths during 627 missions during The In-Situ Aerosol Profiles (IAP) campaign from 2000 to 2006 (https://adc.arm.gov/discovery/#/results/instrument_class_code::iap). The white circle indicates the 15-km distance around the central site (black dot). (B) Vertical profile of aerosol sampling frequency, illustrating the distribution of aerosol measurements across different altitudes above the sea level (a.s.l.) up to 4 km. The bar lengths represent the percentage of samples taken at corresponding altitude during the flight missions.

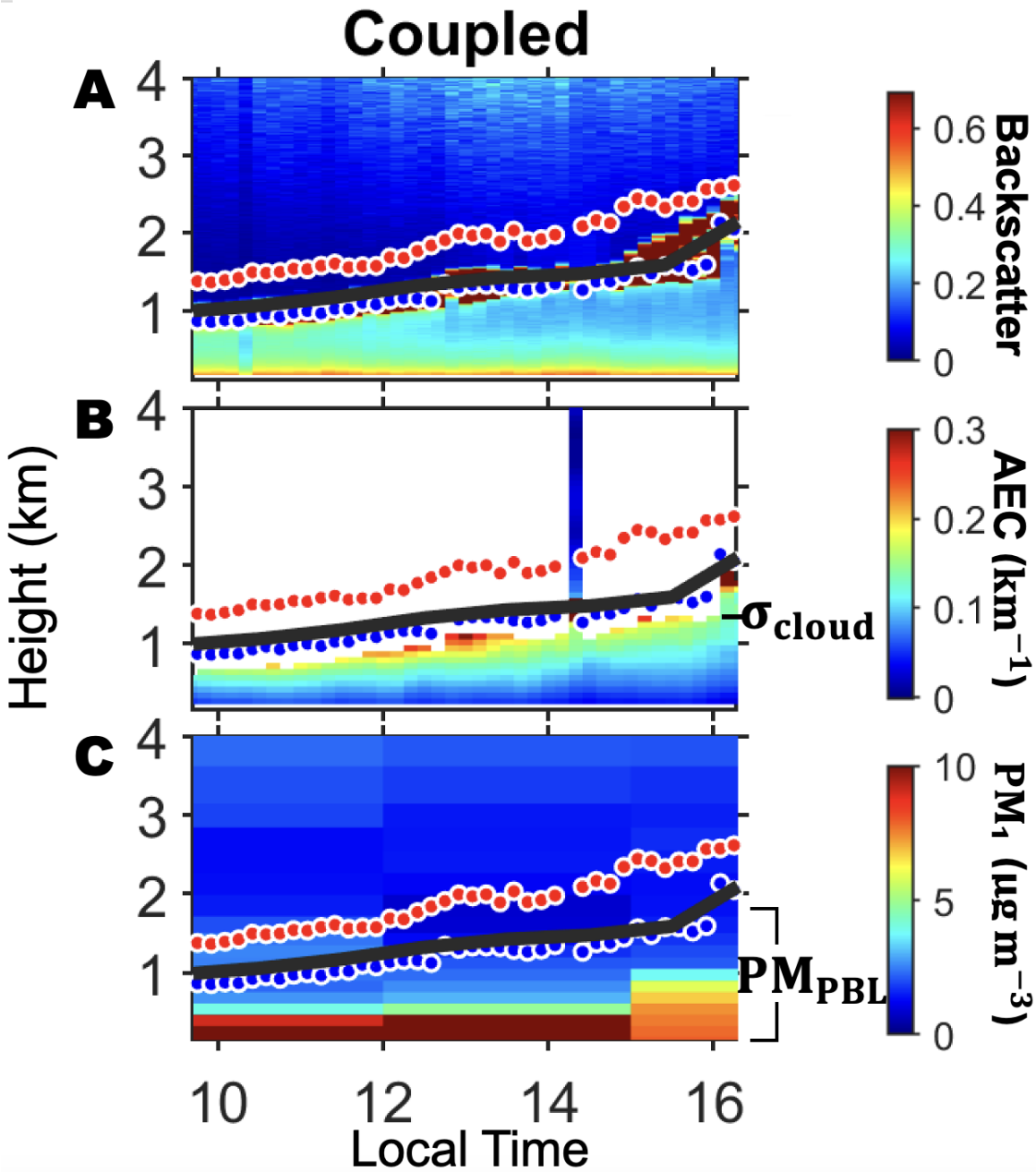

Fig. S2. A coupled cloud case. (A) Lidar backscatter profiles, (B) Aerosol Extinction Coefficients (AEC) profiles derived from Raman Lidar, and (C) PM_1 profiles obtained from MERRA-2. The cloud base and cloud top are represented by blue and red dots, respectively. The position of the PBL top is marked by a black line. σ_{cloud} indicates the aerosol extinction below the cloud base, while PM_{PBL} denotes the mean PM_1 within the PBL.

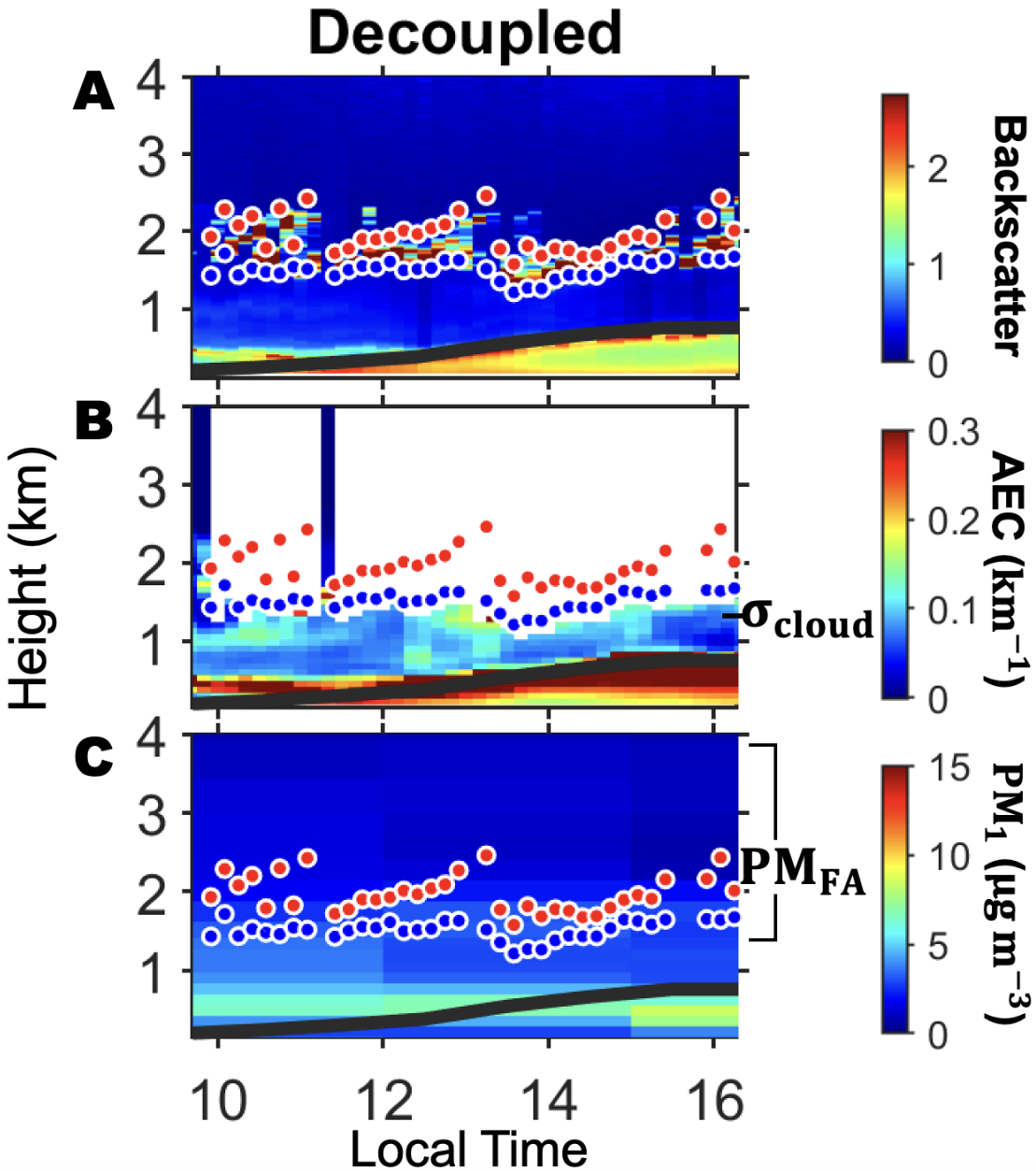

Fig. S3. A decoupled cloud case. (A) Lidar backscatter profiles, (B) Aerosol Extinction Coefficients (AEC) profiles derived from Raman Lidar, and (C) PM_1 profiles obtained from MERRA-2. The cloud base and cloud top are represented by blue and red dots, respectively. The position of the PBL top is marked by a black line. σ_{cloud} indicates the aerosol extinction below the cloud base. PM_{FA} indicates the PM_1 in the free troposphere (FT) and is calculated as the mean value of PM_1 between cloud base and 600 hPa.

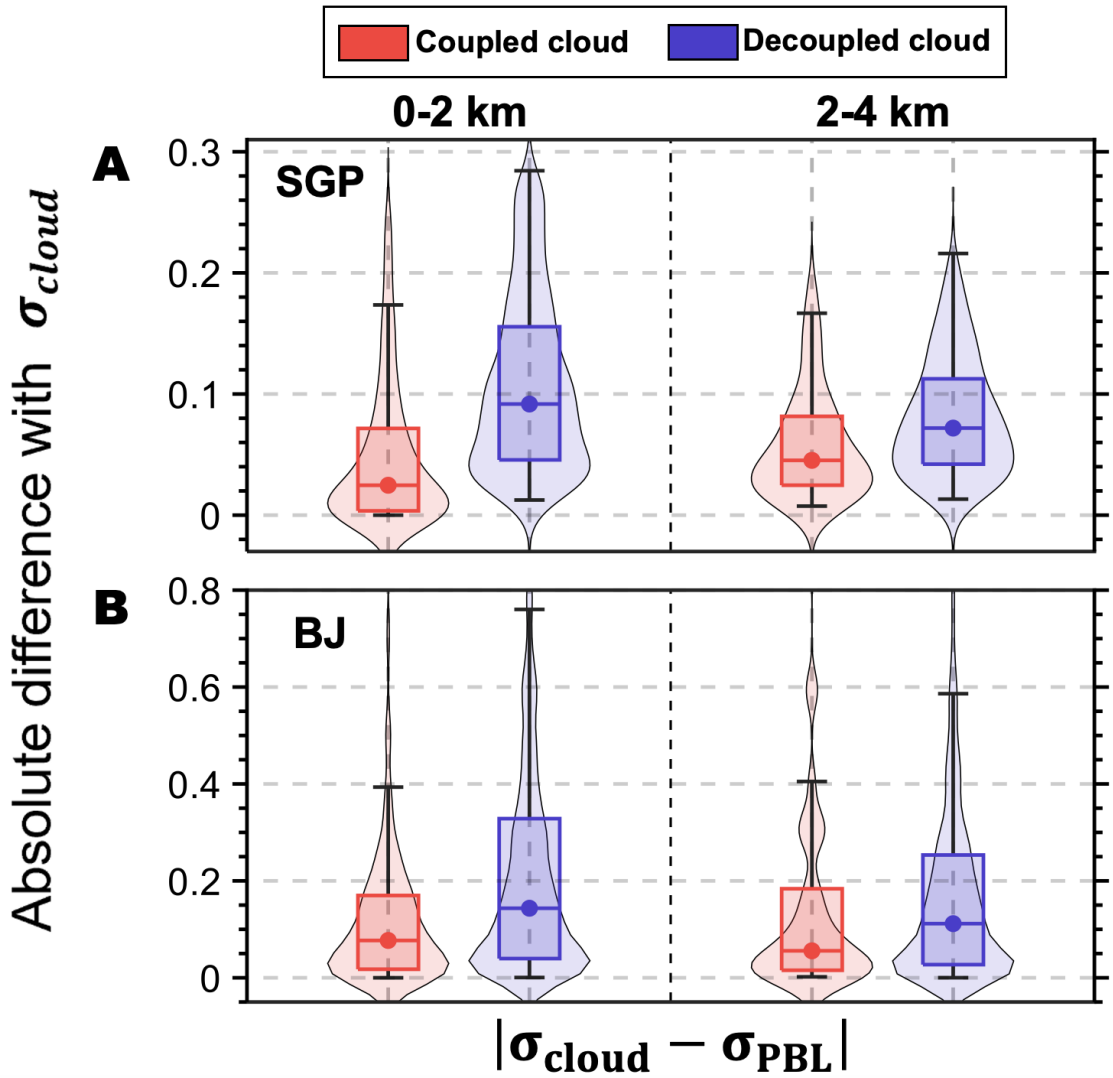

Fig. S4. Sub-cloud aerosol variations under coupled and decoupled regimes. The absolute differences between aerosol extinction (unit: km^{-1}) within boundary layer (σ_{PBL}) and aerosol extinction at the cloud base height (σ_{cloud}) over (A) the SGP site and (B) Beijing. σ_{cloud} is computed as the mean extinction from neighboring clear pixels at the cloud base height. The analysis covers two cloud base ranges: 0-2 km and 2-4 km. Box-and-whisker plots showing the 10th, 25th, 50th, 75th, and 90th percentile values. The width of the color-shaded areas represents the corresponding distribution of absolute differences.

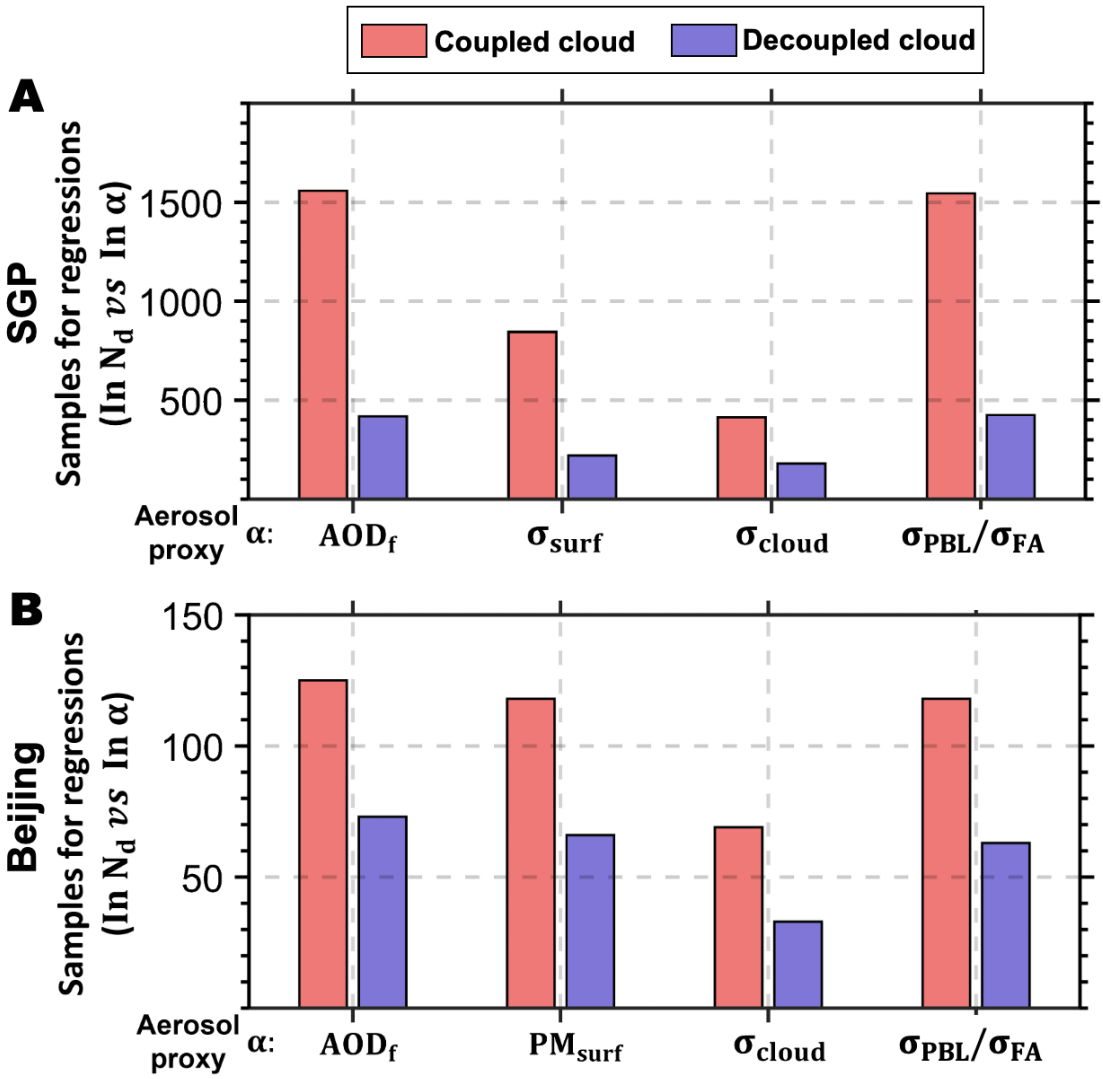

Fig. S5. Number of samples used in regression calculations for both the SGP and Beijing locations. The red bars represent sample counts in hours for the coupled cloud scenario, while the blue bars denote those of the decoupled cloud scenario. Panel (A) showcases samples for SGP, and panel (B) for Beijing. Corresponding regression slopes based on these samples are shown in Figure 2.

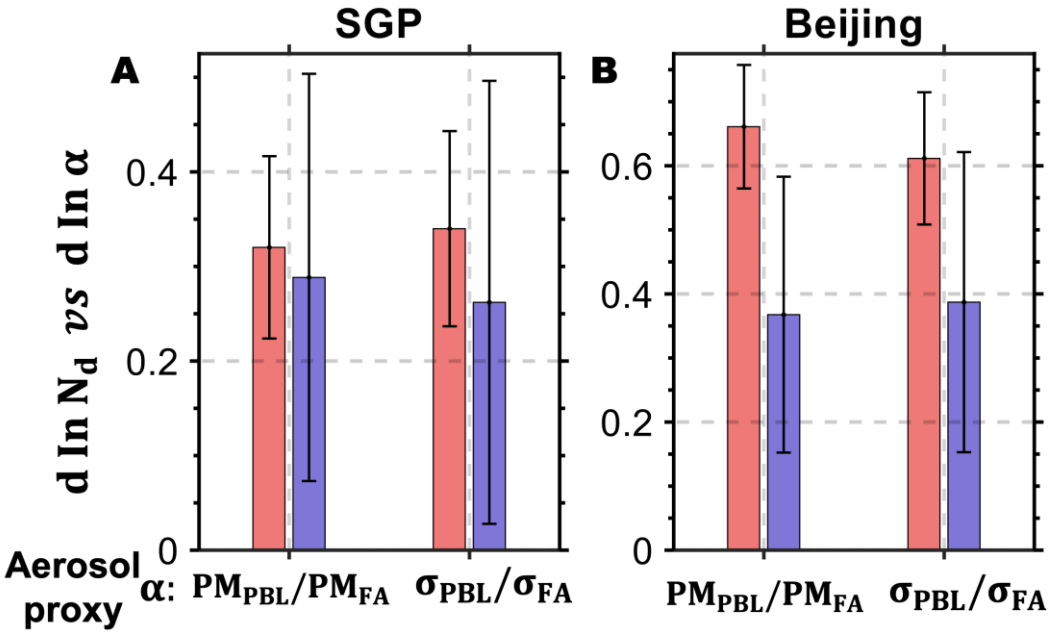

Fig. S6. The responses of cloud droplet number concentration to different aerosol proxies. The responses ($\frac{d\ ln\ N_d}{d\ ln\ \alpha}$) are calculated as the slopes of linear regression between $d\ ln\ N_d$ and $d\ ln\ \alpha$ for liquid water clouds over (A) SGP and (B) Beijing. Red and blue bars indicate the responses for coupled and decoupled cases. The aerosol proxies used are mean PM_1 within PBL (PM_{PBL}) and mean PM_1 within free atmosphere (PM_{FA}), and mean σ_{dry} within PBL (σ_{PBL}) and mean σ_{dry} within free atmosphere (σ_{FA}). The error-bars indicate the 90% confidence level.

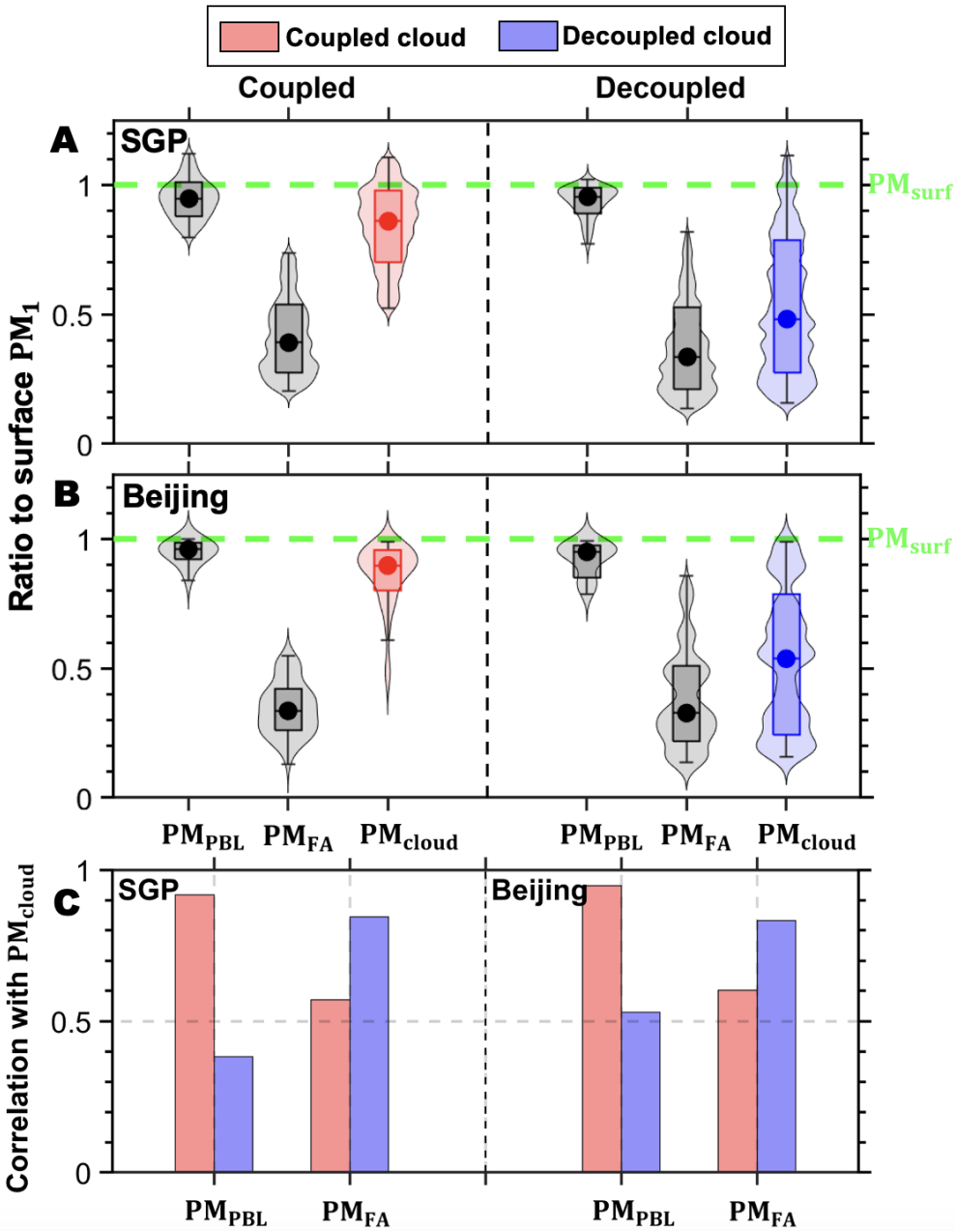

Fig. S7. Values of PM_{PBL} and PM_{FT} over the SGP and Beijing. The ratio between PM_{PBL} and surface PM_1, the ratio between PM_{FA} and surface PM_1, and the ratio between PM_{cloud} and surface PM_1 from MERRA-2 for coupled and decoupled regimes over (A) SGP and (B) Beijing. (C) The correlation coefficients between PM_{cloud} and PM_{PBL}/PM_{FA}.

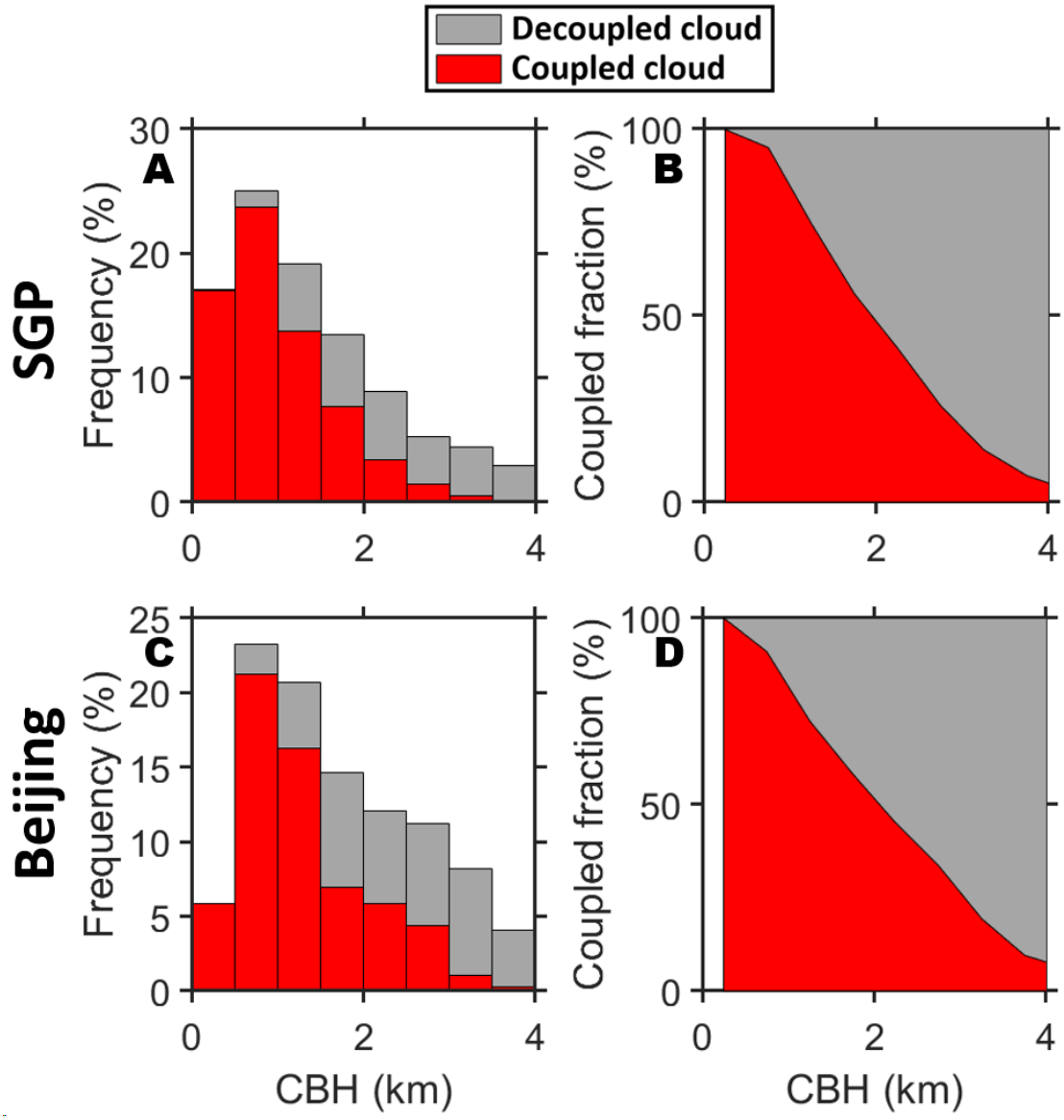

Fig. S8. Climatology and cloud-surface coupling and cloud fraction. The height-dependent occurrence frequencies of the cloud-base height for coupled clouds (red bars) and decoupled clouds (grey bars) over the (A) SGP and (C) Beijing. Panels (B) and (D) represent the coupled fraction (red areas) at different cloud-base heights over the SGP site and Beijing, respectively. Note that only liquid water clouds were considered in this analysis, and instances where coupled and decoupled clouds mixed were excluded.

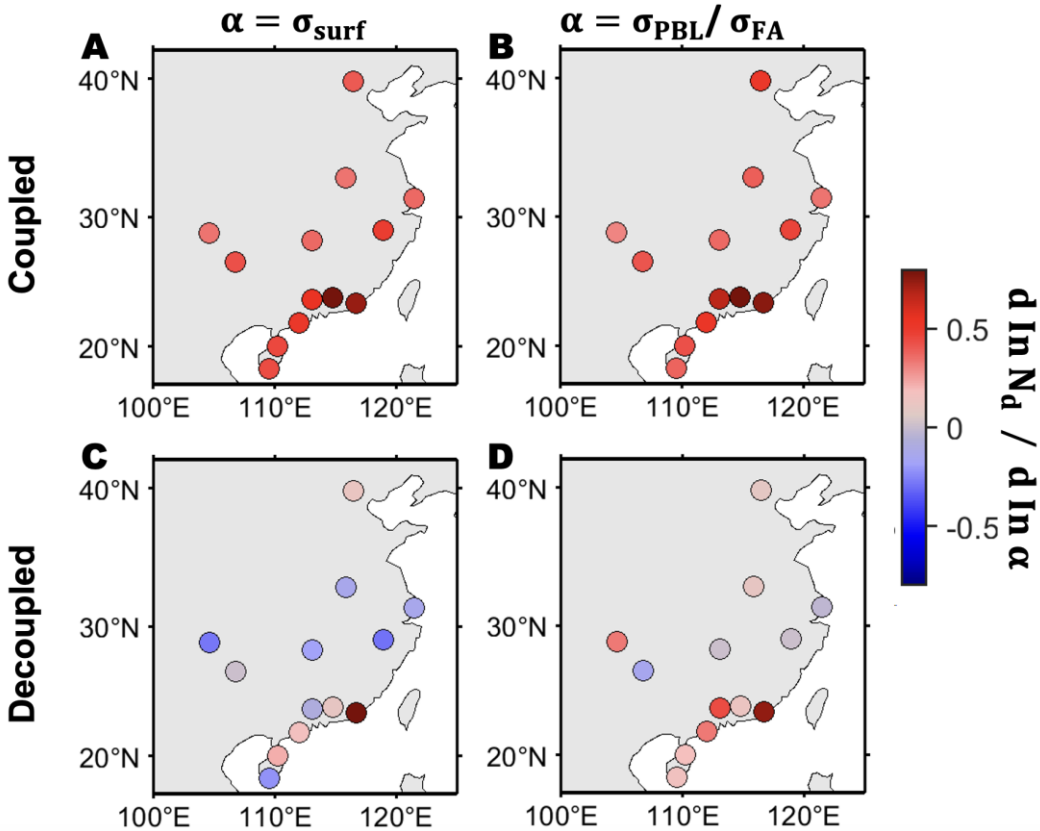

Fig. S9. Responses of cloud droplet number concentration to aerosols. The responses of N_d to aerosols ($\frac{d\ ln\ N_d}{d\ ln\ \alpha}$) is calculated as the slopes of linear regression between $d\ ln\ N_d$ and $d\ ln\ \alpha$ over different radiosonde sites. The aerosol proxies used are surface PM_1 and PM_{PBL}/PM_{FA}. The color shaded dots indicate the value of $\frac{d\ ln\ N_d}{d\ ln\ \alpha}$.

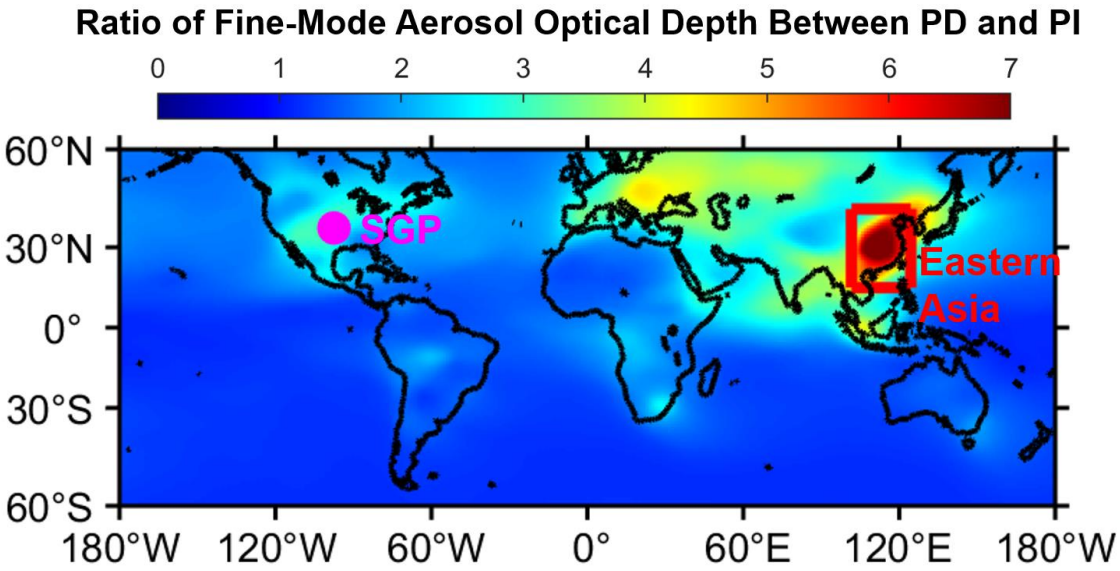

Fig. S10. Comparative Analysis of Fine-Mode Aerosol Optical Depth Between Present Day (2005) and Preindustrial Era (1850). The Fine-Mode Aerosol Optical Depth (AOD_f) for both time periods is derived from the Max Planck Aerosol Climatology version 2 (MACv2). The ratio provides insights into the change in aerosol optical depth from the Preindustrial era to the Present day. Two study regions (SGP and Eastern Asia) have been marked in this Figure.

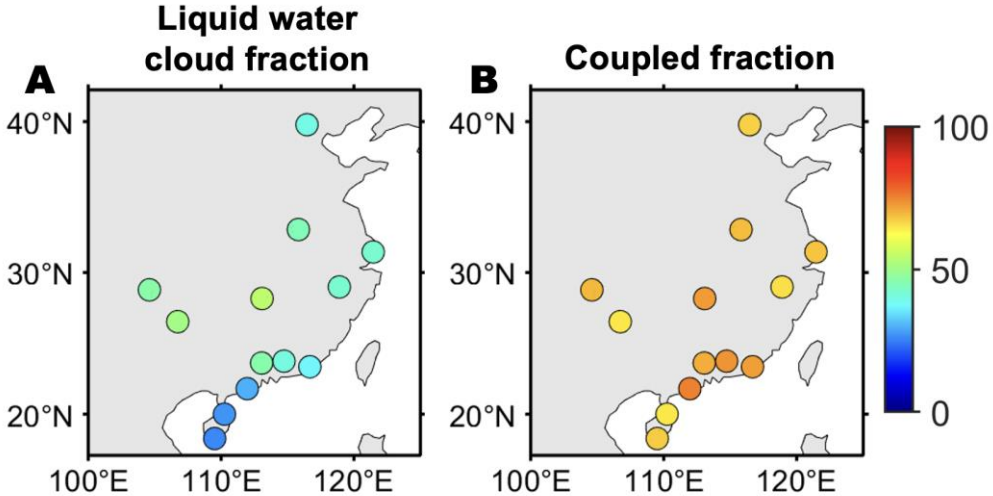

Fig. S11. Cloud fraction and coupled fraction over different radiosonde sites. The color shaded dots indicate the summer mean of (A) liquid water cloud fraction and (B) coupled fraction. The cloud phase is identified by MODIS product, while the cloud-surface coupling is diagnosed by radiosonde profiles.

Table S1. The list of the datasets in the present study, location, periods, and their corresponding description.

Dataset	Location	Period	Description
Beijing Superstation	Beijing, China	July 2017 - October 2019	Observations from a micro-pulse lidar (MPL), surface meteorological instruments, surface PM2.5 observations
Southern Great Plains (SGP)	Oklahoma, USA	October 1998 - December 2020	Measurements of potential temperature, Active Remote Sensing of Clouds, cloud optical properties, radiation budget, and surface aerosol.
In-Situ Aerosol Profiles (IAP) campaign	Oklahoma, USA	2000 - 2006	Dry fine-mode aerosol extinction (diameter<1μm) (σ_{dry}) from the Aerosol Observing System
Radiosonde Stations	Eastern China	Summer 2015 - 2019	Vertical profiles of pressure, water vapor, temperature, and wind at 1400 Local Time.
MODIS Level-2 Cloud	Global	2002-2019	Cloud optical depth, effective radius, top height/temperature, liquid water path, cloud phase, and multilayer flag.
MERRA-2	Global	1998-2020	Re-analyzed AOD_f and vertical profiles of PM_1 at 0.5° x 0.625° resolution.
Max Planck Aerosol Climatology version 2 (MACv2)	Global	N/A	Monthly global maps for aerosol optical properties and compositions with global coverage.